

# Remodeling of Membrane Shape and Topology by Curvature Elasticity and Membrane Tension

Reinhard Lipowsky

Cellular membranes exhibit a fascinating variety of different morphologies, which are continuously remodeled by transformations of membrane shape and topology. This remodeling is essential for important biological processes (cell division, intracellular vesicle trafficking, endocytosis) and can be elucidated in a systematic and quantitative manner using synthetic membrane systems. Here, recent insights obtained from such synthetic systems are reviewed, integrating experimental observations and molecular dynamics simulations with the theory of membrane elasticity. The study starts from the polymorphism of biomembranes as observed for giant vesicles by optical microscopy and small nanovesicles in simulations. This polymorphism reflects the unusual elasticity of fluid membranes and includes the formation of membrane necks or fluid ‘worm holes’. The proliferation of membrane necks generates stable multi-spherical shapes, which can form tubules and tubular junctions. Membrane necks are also essential for the remodeling of membrane topology via membrane fission and fusion. Neck fission can be induced by fine-tuning of membrane curvature, which leads to the controlled division of giant vesicles, and by adhesion-induced membrane tension as observed for small nanovesicles. Challenges for future research include the interplay of curvature elasticity and membrane tension during membrane fusion and the localization of fission and fusion processes within intramembrane domains.

## 1. Introduction

Our body contains a large amount of biomembranes that enclose our cells and many intracellular organelles. These membranes are fluid and create a flexible architecture that partitions each cell into many separate liquid compartments. This membrane architecture is continuously remodeled by two different kinds of processes. First, the flexibility of these membranes allows them to easily adapt their shape to different interactions with

their surroundings. Second, the membrane compartments can change their topology via fusion and fission (or scission) processes. One aspect of these remodeling processes is the heavy trafficking of vesicles between different organelles as displayed in **Figure 1**. This trafficking involves both the production of new vesicles via budding and fission from a donor membrane as well as the uptake of these vesicles by acceptor membranes via adhesion and fusion.

In **Figure 1**, budding processes are emphasized by using different colors for the membrane buds that are formed by different organelles. During such a budding process, the membrane of the organelle forms two interior subcompartments that are connected by a membrane neck. The neck resembles a fluid “worm hole” by which the two subcompartments can exchange both membrane area and liquid volume. To transform the bud into a separate vesicle, the neck must be cleaved which leads to the fission of the organelle and to two separate membrane compartments. In **Figure 1**, the fusion processes correspond to the various arrowheads. In the cell, both fission and

fusion involve a complex assortment of membrane-bound proteins that are believed to steer the different steps of these processes. The different proteins act in a concerted manner which makes it quite difficult to understand their individual roles even during a single fission or fusion event. This complexity is further increased by the multitude of such events that occur simultaneously in a single cell.

The schematic figure in **Figure 1** has been drawn more than a decade ago.<sup>[1]</sup> In the meantime, the membrane architecture of some organelles has been found to be much more complex. One striking example is the endoplasmic reticulum (ER) which is shown in **Figure 1** as a localized stack of membrane sheets. High resolution fluorescence microscopy has revealed, however, that the ER includes a network of membrane nanotubes that spans the whole cell and forms contact sites with all other organelles.<sup>[2,3]</sup> On the other hand, reconstitution experiments have also shown that the reticular network can be formed even in the absence of cytoskeletal filaments.<sup>[4,5]</sup>

New insight into the remodeling of biomembranes can be obtained from the study of synthetic membrane systems which are built up from a relatively small number of molecular components and can be studied in a systematic and quantitative manner. In biochemistry and cell biology, these systems are conventionally called “in vitro” or “reconstituted systems.” Recently, a new motivation for the study of such model systems

R. Lipowsky  
Theory & Biosystems  
Max Planck Institute of Colloids and Interfaces  
Science Park Golm  
Potsdam, Germany  
E-mail: lipowsky@mpikg.mpg.de

 The ORCID identification number(s) for the author(s) of this article can be found under <https://doi.org/10.1002/adbi.202101020>.

© 2021 The Authors. Advanced Biology published by Wiley-VCH GmbH. This is an open access article under the terms of the Creative Commons Attribution-NonCommercial License, which permits use, distribution and reproduction in any medium, provided the original work is properly cited and is not used for commercial purposes.

DOI: 10.1002/adbi.202101020

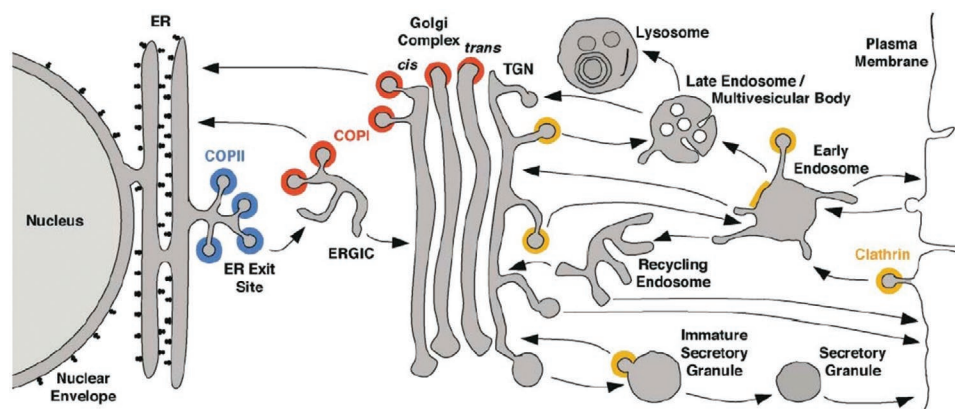


**Figure 1.** Vesicle trafficking between different organelles within an animal cell: the vesicles are formed by budding and fission from different membrane-bound organelles. The different colors (blue, red, yellow) are used to distinguish bud formation from different donor membranes. The arrowheads indicate adhesion and fusion events between a vesicle and an acceptor membrane. Reproduced with permission.<sup>[1]</sup> 2004, Elsevier.

has been provided by the emerging bottom-up approach to synthetic biology because biomembranes represent an important module for this approach. The present paper reviews some contributions to this latter research activity.

Two synthetic model systems will be discussed as provided by giant vesicles and small nanovesicles. The methodology will be based on the integration of experimental observations of giant vesicles by optical microscopy, molecular dynamics simulations of small nanovesicles, and the theory of membrane elasticity, which involves both curvature elasticity and membrane tension. The remodeling of giant vesicles, which have a typical size of many micrometers, has been studied for a long time.<sup>[6–9]</sup> Using optical microscopy, one can both image the vesicle morphology and monitor the transformations between these morphologies. The morphology of small nanovesicles, on the other hand, cannot be resolved by optical microscopy. Therefore, small nanovesicles have been traditionally imaged by different variants of electron microscopy.<sup>[10–15]</sup> The latter methods are, however, restricted to a single snapshot of each nanovesicle and, thus, cannot monitor how the shape of such a vesicle changes with time. These shape transformations of nanovesicles are, however, accessible to molecular dynamics simulations as has been recently demonstrated.<sup>[16,17]</sup>

This paper is organized as follows. Section 2 provides a showcase for the shapes of both giant vesicles and small nanovesicles, focusing on shapes that involve membrane necks. These necks lead to intriguing remodeling processes of membrane shape and are also essential for the remodeling of membrane topology. Section 3 summarizes the theory for membrane elasticity, which deals with two types of elastic deformations, membrane stretching (or compression) and membrane bending. In addition, Section 3 contains subsections on the local generation of spontaneous curvature, on the spontaneous tension which is intimately related to the spontaneous curvature, and on the composite nature of membrane tension. Two important aspects of tension are that the tension of a bilayer can be decomposed into a mechanical and a spontaneous tension and that the mechanical bilayer tension can be further divided up into two leaflet tensions.

In Section 4, the local properties of membrane necks are discussed which include the local stability of closed necks and

the curvature-induced constriction forces that act to squeeze the necks. Section 5 is devoted to two-sphere vesicles which provide the simplest example for multispherical shapes and should be considered to provide a case study. The results of this section are generalized in Section 6 to multispherical shapes that consist of an arbitrary number of large and small spheres. Finally, in Section 7, the remodeling of membrane topology, which is based on fission and fusion events, will be addressed.

## 2. Remodeling of Membrane Shape

Biomembranes are fluid and can easily adapt their shape to changing cues in their environment. In this section, we will provide several examples for the morphological responses of biomembranes and vesicles that do not involve topological transformations via membrane fusion or membrane fission. However, even in the absence of such processes, the shape remodeling of a biomembrane can generate several subcompartments via the formation of membrane necks.

### 2.1. Membrane Compartments In Vivo and In Vitro

Cellular membranes form a large variety of different compartments. Each cell is enclosed by a plasma membrane which provides the boundary between the cell and its surroundings. In addition, the eukaryotic cells of animals and plants contain a large number of intracellular membranes that enclose different organelles as in Figure 1. The cellular membranes differ greatly in their lateral extensions, from many tens of micrometers for plasma membranes to small nanovesicles such as synaptic vesicles with a diameter that varies between 20 and 50 nm<sup>[18,19]</sup> as well as exosomes, which represent small extracellular vesicles with a diameter between 25 and 100 nm.<sup>[20–22]</sup> In recent years, exosomes and somewhat larger extracellular vesicles have been intensely studied as possible biomarkers for diseases and as targeted drug delivery systems.<sup>[23–26]</sup>

Cellular membranes can attain a striking variety of different shapes. The plasma membrane of a red blood cell, for instance, has a characteristic discocyte shape whereas the plasma membrane of a white blood cell typically forms long membrane

protrusions that can explore a large spatial region around the cell. Particularly intriguing morphologies are observed for the plasma membranes of neurons, which form complex dendritic trees as well as rather long axons. Likewise, membrane-bound organelles can have rather striking shapes. One example is provided by the endoplasmic reticulum which is displayed in Figure 1 in a very simplified manner because we now know that it includes a network of membrane nanotubes that spans the whole cell.<sup>[5,27]</sup>

Many of the membrane processes *in vivo* can also be studied *in vitro* using synthetic or reconstituted membrane compartments. These compartments are based on lipid bilayers which form closed vesicles. For these lipid vesicles, a variety of methods has been developed by which one can vary their size over a wide range, from a few tens of nanometers to many tens of micrometers. In the literature, three different types of lipid vesicles are usually distinguished: small unilamellar vesicles (SUVs) with a diameter below 50 nm; large unilamellar vesicles (LUVs) with a typical size between 100 and 200 nm; and giant unilamellar vesicles (GUVs), the size of which exceeds one micrometer but can be as large as 100  $\mu\text{m}$ . In the following, we will only discuss membrane compartments that are formed by a single bilayer membrane. Therefore, we will often omit the term “unilamellar” and refer to SUVs, LUVs, and GUVs as small nanovesicles, large nanovesicles, and giant vesicles, respectively.

## 2.2. Giant Vesicles with Membrane Necks

Giant vesicles provide a direct connection between the nano- and the microregime. On the one hand, these vesicles represent biomimetic compartments with linear dimensions of many micrometers. On the other hand, the vesicle walls are provided by single molecular bilayers that have a thickness of a few nanometers and respond sensitively to molecular interactions with small solutes, biopolymers, and nanoparticles. These nanoscopic responses are amplified by the giant vesicles and can then be studied on much larger scales by optical microscopy. Therefore, giant vesicles have been increasingly used as a versatile research tool for basic membrane science, bioengineering, and synthetic biology. Here, we will focus on the polymorphism of giant vesicles that has been studied for quite some time. In the following, we will illustrate this polymorphism with a few selected examples, all of which involve the formation of membrane necks which provide “worm holes” between two aqueous subcompartments enclosed by two membrane segments.

### 2.2.1. Budded Vesicles with a Single Membrane Neck

One shape transformation of giant vesicles that has been frequently observed is the budding of these vesicles which leads to the formation of a small spherical bud, connected to the mother vesicle by a single membrane neck or “worm hole.” One example for such a budding process is displayed in Figure 2. In this example, the vesicle was prepared in an aqueous solution of sucrose and then transferred to an observation chamber in which the osmolarity of the exterior solution was increased by adding glucose. This procedure had two consequences. First, the increased osmolarity reduced the volume of the vesicle. Second, the lipid bilayer now acquired a transbilayer asymmetry because the inner leaflet of this bilayer was still exposed to sucrose whereas the outer leaflet was now in contact with glucose. The combination of volume reduction and transbilayer asymmetry induced the shape transformation from the initial pear-like shape to a budded shape, consisting of two (punctured) spheres that are connected by a closed membrane neck, as displayed in Figure 2. In this example, the whole transformation from the pear-like to the two-sphere shape took about 16 s.

The transbilayer asymmetry leads to a preferred curvature of the vesicle membrane, the so-called spontaneous curvature. This curvature can be directly estimated from the inverse size of the spherical bud. If this bud has a radius of about 1  $\mu\text{m}$ , the spontaneous curvature is about 1  $\mu\text{m}^{-1}$ . Furthermore, the theory of curvature elasticity predicts that an outward budding process as in Figure 2 can only occur if the preferred or spontaneous curvature of the membrane exceeds a certain threshold value and that this threshold value depends on the volume of the vesicle and on the area of the vesicle membrane. Therefore, for a given membrane area, the bud size depends on the vesicle volume and on the spontaneous curvature. The vesicle volume is relatively easy to control by changing the osmotic conditions while fine-tuning of the spontaneous curvature is more difficult to achieve.

An unprecedented control of the spontaneous curvature has been recently accomplished by low densities of membrane-bound proteins as shown in Figure 3.<sup>[29]</sup> The giant vesicles were exposed to nanomolar concentrations of His-tagged GFP in the exterior buffer solution. The His-tagged proteins were bound to certain anchor lipids in the outer leaflet of the vesicle membrane. The density of membrane-bound protein increased linearly with the nanomolar concentration in the exterior buffer. As a consequence, the spontaneous curvature was found to increase linearly with the GFP concentration as well. Thus, the size of the bud could be controlled by changing both the vesicle

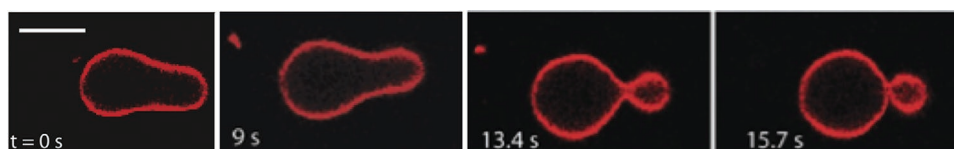


**Figure 2.** Budding of a giant vesicle, eventually creating two interior subcompartments, which are connected by a closed membrane neck or “worm hole.” The first snapshot defines the time point at which the imaging was started; the three subsequent snapshots represent the time lapse of an individual vesicle and were taken after 9, 13.4, and 15.7 s. The scale bar in the first panel is 5  $\mu\text{m}$  and applies to all panels. Reproduced under terms of the CC-BY license.<sup>[28]</sup> Copyright 2019, The Authors, published by Royal Society of Chemistry.

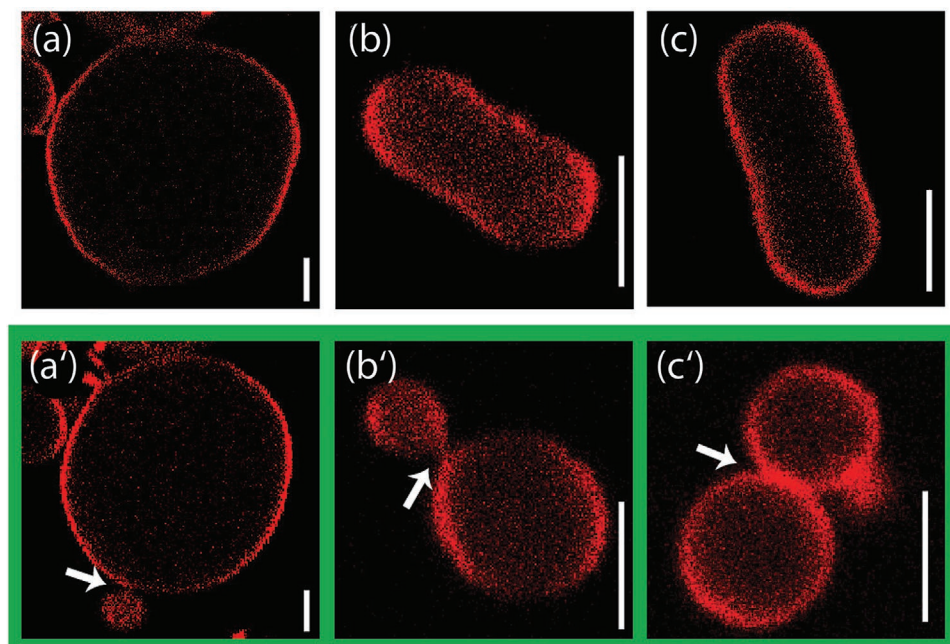


**Figure 3.** Controlled budding of giant vesicles: Two parameters were used to steer the budding transformations and to control the size of the bud. First, the vesicle volume was varied in the absence of His-tagged proteins by changing the osmotic conditions, as shown in panels a–c. Second, the spontaneous curvature of the membranes was controlled by the molar concentration of His-tagged GFP in the exterior buffer. When this molar concentration was increased from zero in panels (a–c) to finite values in panels (a'), (b'), and (c'), buds of different sizes were formed. The white arrows indicate the positions of the membrane necks. All scale bars: 5  $\mu\text{m}$ . Reproduced under terms of the CC-BY license.<sup>[29]</sup> Copyright 2020, The Authors, published by Springer Nature.

volume and the concentration of the His-tagged proteins in the exterior buffer.

### 2.2.2. Giant Vesicles with Lipid Phase Domains

Many lipid mixtures phase separate into two lipid phases, a liquid-ordered and a liquid-disordered phase, which are both fluid and form large intramembrane domains.<sup>[30–33]</sup> These domains are separated by a domain boundary which has a line energy that is proportional to the length of this boundary.<sup>[34,35]</sup> The budding process is facilitated by these domain boundaries as shown in **Figure 4**, where different membrane dyes have been used to distinguish the two types of domains via fluorescence microscopy.<sup>[32,36,37]</sup>

### 2.2.3. Active Shape Oscillations

In the previous examples, the formation of a membrane neck was observed during the relaxation of the vesicle shape toward a (meta)stable state. Recently, shape oscillations of giant vesicles have been observed,<sup>[38]</sup> during which the vesicles changed their neck size in a recurrent manner.<sup>[39]</sup> These oscillations are caused by Min proteins that attach to and detach from the vesicle membranes,<sup>[40]</sup> with the detachment being driven by ATP hydrolysis. The observed shape oscillations can be understood in terms of a spontaneous curvature that undergoes cyclic changes in time.<sup>[39]</sup> During each oscillation cycle, the vesicle shape is transformed from a symmetric dumbbell with two equally sized

subcompartments to an asymmetric dumbbell with two subcompartments that differ in their size, followed by the reverse, symmetry-restoring transformation, as displayed in **Figure 5**. Inspection of this figure shows that the dumbbells possess membrane necks that close and open up during each oscillation cycle.

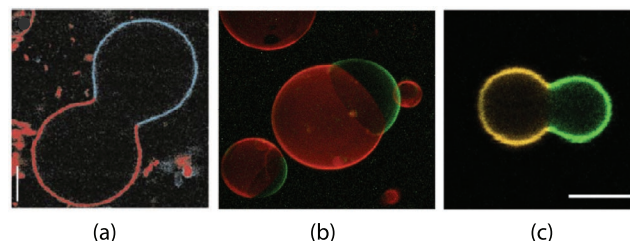


**Figure 4.** Domain-induced budding of giant vesicles as predicted by theory<sup>[34,35]</sup> and observed by fluorescence microscopy.<sup>[32,36,37]</sup> The two intramembrane domains consist of liquid-disordered (Ld) and liquid-ordered (Lo) lipid phases: a) Cross-section through a vesicle that formed two lipid phase domains after a decrease in temperature;<sup>[32]</sup> b) 3D confocal scan of a two-domain vesicle that was formed by electrofusion;<sup>[36]</sup> and c) Cross-section through a two-domain vesicle after osmotic deflation.<sup>[37]</sup> In each example, two different membrane dyes have been used to distinguish the Ld and Lo domains by fluorescence microscopy. The Ld phase is red in (a,b) and orange in (c), the Lo phase is blue in (a) and green in (b,c). Because the line tension of a domain boundary is positive, this boundary can reduce its line energy by constricting the vesicle to form a membrane neck. Scale bars: 5  $\mu\text{m}$  in (a) and 10  $\mu\text{m}$  in (c). Panel (a) reproduced with permission.<sup>[32]</sup> 2003, Springer Nature. Panel (b) reproduced with permission.<sup>[36]</sup> Copyright 2016, published by World Scientific Publishing Co Pte Ltd. Panel (c) reproduced under terms of the CC-BY license.<sup>[37]</sup> Copyright 2020, The Authors, published by Wiley-VCH.

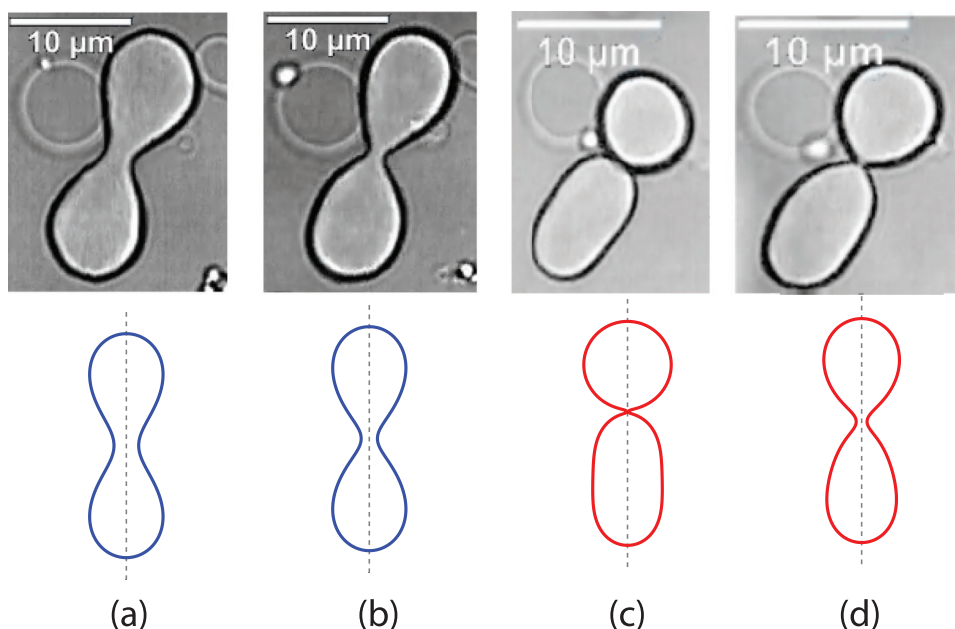


**Figure 5.** Active shape oscillations of a giant vesicle that encloses Min proteins and ATP as observed experimentally<sup>[38]</sup> and computed from the theory of curvature elasticity.<sup>[39]</sup> The theory reveals that the shape oscillations of the vesicle can be understood in terms of a time-dependent spontaneous curvature that arises from the cyclic binding and ATP-driven unbinding of the proteins to and from the vesicle membrane. In this example, 26 such cycles with an average cycle time of 56 s have been observed. Reproduced under terms of the CC-BY license.<sup>[39]</sup> Copyright 2021, The Authors, published by Royal Society of Chemistry.

In the example shown in Figure 5, 26 such oscillations have been observed, with an average cycle time of 56 s.

#### 2.2.4. Multispherical Vesicles with Many Necks

The vesicle shapes in Figures 2–5 involve a single membrane neck. These shapes represent the simplest examples for stable multispherical or “multi-balloon” shapes. Indeed, the theory of curvature elasticity predicts that vesicles can form multispherical shapes consisting of an arbitrary number of large and small spheres that are connected by closed membrane necks. One remarkable feature of these multispheres is that they can involve only two different sphere radii, which define the large and small spheres.

A recent experimental study has demonstrated that stable multispherical shapes can indeed be formed by giant vesicles, see **Figure 6**. Each multisphere in this figure has a complex morphology consisting of several spheres and several membrane necks. Furthermore, it is important to note that each of these multispherical shapes is formed by a single membrane. The properties of such multispheres will be discussed further below, together with additional microscopy images that display multispheres that involve even larger numbers of spheres.

### 2.3. Membrane Necks at the Nanoscale

The shape of nanovesicles with a diameter below 300 nanometers cannot be imaged by conventional optical microscopy. Therefore, a variety of electron microscopy (EM) methods has been used to image these vesicles, but all EM methods are

restricted to a single snapshot of each nanovesicle and, thus, cannot monitor how the shape of such a vesicle changes with time. These shape transformations of nanovesicles are, however, accessible to molecular dynamics simulations.<sup>[16,17,41–45]</sup> Here, we focus on two recent simulations<sup>[16,17]</sup> which revealed that the leaflet tensions and the concentrations of small solutes, which adsorb onto the membranes, represent important control parameters for the nanovesicle morphologies, see **Figure 7** and Section 7.3 further below. In particular, these studies identified parameter values for the formation of membrane necks. Furthermore, during the engulfment of small nanodroplets, membranes can form non-circular necks that arise from the negative line tension of the contact line between nanodroplet and membrane,<sup>[46]</sup> see **Figure 8**.

#### 2.3.1. Budding of Small Nanovesicles

To study the shape transformations of lipid nanovesicles, we started with the assembly of spherical vesicles that enclose a certain volume of water and contain a certain total number of lipids, see the leftmost snapshots in Figure 7. When we reduce their volume, the spherical vesicles are observed to transform into a multitude of nonspherical shapes such as oblates and stomatocytes as well as prolates and dumbbells. Two examples of these shape transformations are displayed in Figure 7. In panel (a) of this figure, the initially spherical vesicle transforms into a stomatocyte with an inward-pointing bud; in panel (b), the spherical nanovesicle transforms into a dumbbell with an outward-pointing bud and a closed neck.

The different shape transformations of these nanovesicles can be controlled by the transbilayer distribution of the

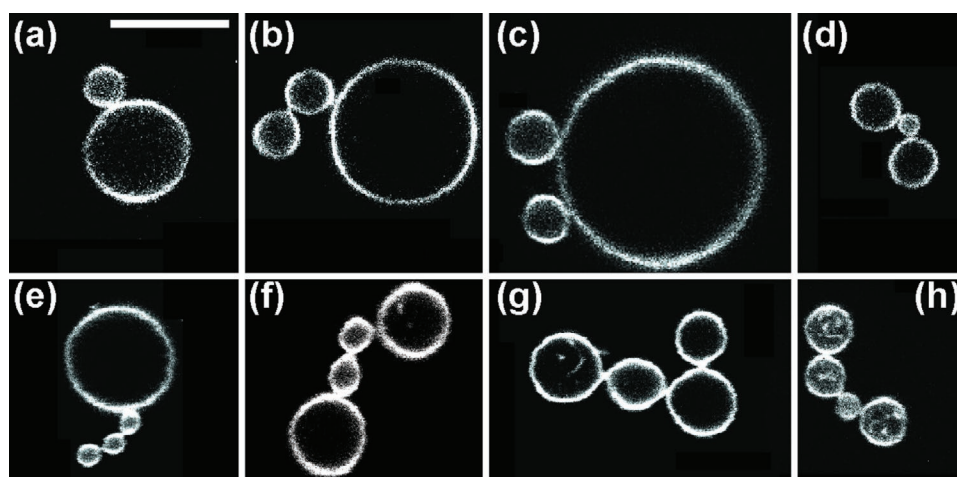


**Figure 6.** Multispherical shapes of giant vesicles with a total number of up to four spheres as observed by optical microscopy. Each multisphere involves only two different sphere sizes as predicted by the theory of curvature elasticity: a) One large and one small sphere as in Figure 2; b,c) Multispheres consisting of one large and two small spheres, forming two distinct patterns; d) A small sphere in between two large spheres; e) One large sphere connected to a linear tubule of three small spheres; f,g) Two large spheres and two small spheres forming two distinct patterns of necklaces; and h) A necklace formed by three large spheres and one small sphere. The scale bar in (a) is 10  $\mu\text{m}$  and applies to all panels. Reproduced under terms of the CC-BY license.<sup>[28]</sup> Copyright 2020, The Authors, published by Royal Society of Chemistry.

assembled lipid molecules. Thus, the two spherical vesicles shown in Figure 7a,b are built up from the same total number of lipid molecules but differ slightly in the lipid numbers assembled in the inner and outer leaflet of the bilayer membrane. In fact, redistributing only 2% of the lipids between the two leaflets of the spherical vesicle leads to very different shape transformation during the reduction of the vesicle volume. This sensitivity to small changes in the assembled lipid numbers arises from different mechanical tensions within the two bilayer leaflets. Thus, the formation of the inward-pointing bud in Figure 7a is caused by the initial stretching of the outer leaflet and the initial compression of the inner leaflet. Likewise, the formation of the outward-pointing bud in Figure 7b is caused by the initial compression of the outer leaflet and the initial stretching of the inner leaflet.

### 2.3.2. Membrane Engulfment of Liquid Droplets

So far, we have tacitly assumed that the membrane necks are axisymmetric, in accordance with the giant vesicle experiments, see Figures 2–5, and with the molecular dynamics simulations in Figure 7. One process, for which non-axisymmetric membrane necks have been observed, is the engulfment of small nanodroplets, as illustrated in Figure 8. In this case, the engulfment process was controlled by the mechanical tension in the lipid bilayer which was steered by the extension of the simulation box parallel to the membrane. We considered a bilayer membrane assembled with a certain, fixed number of lipids, and reduced the mechanical bilayer tension by decreasing the parallel box extension  $L_{\parallel}$ , while keeping the box volume constant.

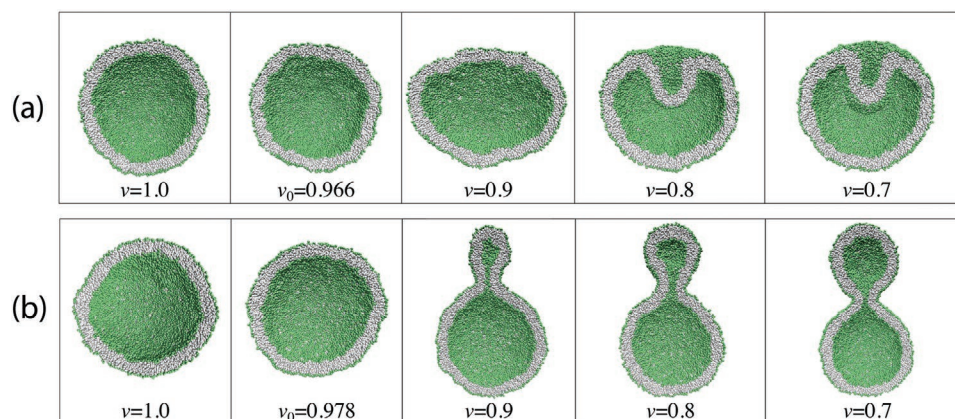


**Figure 7.** Budding of nanovesicles as observed in molecular dynamics simulations.<sup>[16]</sup> Each snapshot displays half a vesicle, with the cross-section across the hydrophobic core of the bilayer membrane in grey and the lipid head groups in green. The budding transformations were induced by decreasing the volume  $v$  of the two spherical vesicles with  $v = 1$ . For  $v = v_0$ , the vesicle membranes have zero bilayer tension. The direction of budding was controlled by the two leaflet tensions of the spherical bilayer: a) Formation of an inward-pointing bud for a spherical vesicle with a compressed inner and a stretched outer leaflet; and b) Formation of an outward-pointing bud for a spherical vesicle with a compressed outer and a stretched inner leaflet. Reproduced under terms of the CC-BY license.<sup>[16]</sup> Copyright 2019, The Authors, published by American Chemical Society.

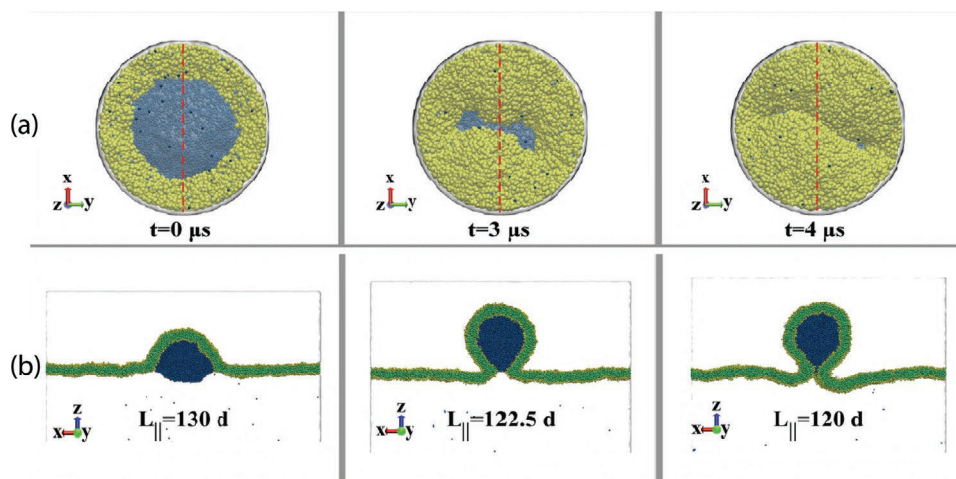


**Figure 8.** Time evolution of a membrane neck generated by a nanodroplet (blue) that adheres to the membrane.<sup>[46]</sup> The head groups and the hydrocarbon chains of the lipids are yellow and green, respectively: a) Bottom views of circular membrane segments (yellow) around the droplet's interface (blue), separated by the contact line which is circular at  $t = 0 \mu\text{s}$ , strongly non-circular after  $t = 3 \mu\text{s}$ , and has closed into a tight-lipped shape after  $t = 4 \mu\text{s}$ ; and b) Side views of the same membrane-droplet morphologies, with perpendicular cross-sections through membrane (green) and droplet (blue) taken along the red dashed lines in panel (a). The non-circular shape of the membrane neck is caused by the negative line tension of the contact line. Reproduced under terms of the CC-BY license.<sup>[46]</sup> Copyright 2018, The Authors, published by American Chemical Society.

Initially, at time  $t = 0 \mu\text{s}$ , we chose  $L_{||} = 130 d$  with the basic length scale provided by the bead diameter  $d = 0.8 \text{ nm}$ . For this initial  $L_{||}$ -value, the lipid bilayer experienced a relatively high bilayer tension, for which the droplet formed a circular contact line with the membrane, see leftmost snapshots in Figure 8. We then reduced  $L_{||}$  from  $130 d$  to  $120 d$  over the next 4 ms, thereby reducing the mechanical bilayer tension acting on the membrane. During the initial reduction of the membrane tension, the droplet-bilayer morphology remained axisymmetric and the contact line retained its circular shape. However, when we reached a certain threshold value of the mechanical tension, the system underwent an unexpected transition to a non-axisymmetric morphology, accompanied by strong shape fluctuations. As we further reduced the membrane tension, the non-axisymmetric morphology persisted until the nanodroplet was completely engulfed by the membrane and the membrane neck had been closed into an unusual, tight-lipped shape, see rightmost snapshots in Figure 8. A detailed analysis of the force balance along the contact line revealed that this unusual neck morphology is caused by the negative line tension of the contact line.

The process displayed in Figure 8 provides one example for the wetting and molding of membranes by liquid droplets. Such wetting and molding processes are not limited to nanodroplets but can also occur for any kind of droplets that are formed by phase separation of an aqueous solution. Examples for this kind of phase behavior are aqueous two-phase systems,<sup>[47]</sup> water-in-water emulsions,<sup>[48]</sup> and biomolecular condensates.<sup>[49,50]</sup> So far, wetting and molding phenomena have been studied in some detail for GUVs exposed to aqueous two-phase systems<sup>[51,52]</sup> and have also been observed for GUVs and biomolecular condensates. A detailed theory for these phenomena has been developed in refs. [53,54].

### 3. Elasticity of Biomembranes

All biomembranes contain a lipid bilayer in its fluid state. On the molecular scale, this fluidity implies that two neighboring lipids swap their relative positions within nanoseconds. On the supra-molecular scale, fluid membranes have no shear modulus, that is, no elastic-restoring force against shear deformations. As a consequence, the shape of these membranes is governed by bending and stretching deformations. In this section, we will focus on the stable morphologies of membranes and vesicles for which the effects of shape undulations are small and can be largely ignored. This assumption is justified as long as the bending rigidity  $\kappa$  of the membranes is large compared to the thermal energy  $k_B T$ . For a phospholipid bilayer, a typical value for  $\kappa$  is  $20 k_B T$  or about  $0.8 \times 10^{-19} \text{ J}$  at room temperature  $T = 25 \text{ }^\circ\text{C}$ .<sup>[55]</sup>

#### 3.1. Elastic Deformations of Fluid Membranes

##### 3.1.1. Stretching and Compression of Membranes

One important quantity that characterizes the geometry of a membrane is its surface area,  $A$ . In the absence of external constraints or forces, the membrane is tensionless and attains its optimal area,  $A = A_0$ . In general, the membrane area  $A$  differs from its optimal value and then experiences the mechanical tension

$$\Sigma(A) = K_A \frac{A - A_0}{A_0} \quad (1)$$

which is proportional to the area dilation  $(A - A_0)/A_0$ . A positive membrane tension,  $\Sigma > 0$ , leads to an increase of the membrane area with  $A - A_0 > 0$  and, thus, to membrane stretching.

A negative membrane tension,  $\Sigma < 0$ , on the other hand, implies that  $A - A_0 < 0$  and that the membrane is compressed.

For lipid bilayers, the area compressibility modulus  $K_A$  is typically of the order of 100 to 300 mN m<sup>-1</sup> as has been measured by micropipette experiments.<sup>[56]</sup> This value should be compared with the rupture tension which is typically 5 to 10 mN m<sup>-1</sup>. Because the area compressibility modulus is much larger than the rupture tension, the area dilation  $(A - A_0)/A_0$  is limited to a few percent before the membrane ruptures. Therefore, we can indeed ignore nonlinear contributions to the tension which are of higher order in the area dilation, which justifies the linear relationship in Equation (1).

The elastic stretching energy is then given by

$$E_{st} = \int_{A_0}^A dA' \Sigma(A') = \frac{1}{2} K_A \frac{(A - A_0)^2}{A_0} \quad (2)$$

which is always positive and represents the reversible work that we have to perform in order to stretch or compress the membrane from its optimal area  $A_0$  for zero tension.

### 3.1.2. Bending Deformations and Curvature

Bending deformations are intimately related to membrane curvature. We now view the membrane as a smoothly curved surface which implies that each point of this surface can be characterized by two principal curvatures,  $C_1$  and  $C_2$ . These principal curvatures can be constructed, in a pedestrian manner, by the following procedure. First, we consider all normal sections through the surface which contain both the point P under consideration and the normal vector erected at this point. The intersection of each normal section with the membrane surface defines a cross-sectional curve which has a certain curvature,  $C$ , at point P. When we rotate the normal section around the normal vector, the curvature  $C$  varies smoothly within a certain interval,  $C_{min} \leq C \leq C_{max}$ . The extremal values,  $C_{min}$  and  $C_{max}$ , define the principal curvatures<sup>[57,58]</sup>  $C_1$  and  $C_2$  at the chosen point P as well as the mean curvature  $M$  and the Gaussian curvature  $G$  via

$$M \equiv \frac{1}{2}(C_1 + C_2) \quad \text{and} \quad G \equiv C_1 C_2 \quad (3)$$

The principal curvatures are local geometric quantities which vary along the membrane which implies that both the mean and the Gaussian curvatures are local geometric quantities as well. It is important to note that all curvatures can be positive or negative which will play an important role for the stability of membrane necks as explained further below.

The simplest model for the curvature elasticity of a biomembrane is the so-called spontaneous curvature model,<sup>[59,60]</sup> for which the bending energy of a curved membrane has the form

$$E_{be} = \int dA 2\kappa(M - m)^2 \quad (4)$$

which involves two material parameters, the bending rigidity  $\kappa$  and the spontaneous curvature  $m$ . Here, we have focused on membrane compartments and vesicles with a certain fixed

topology, which applies to all vesicle morphologies displayed in Figures 2–6. In such a situation, the elastic energy does not involve the Gaussian curvature  $G$  which will, however, become important for remodeling of the membrane topology as discussed further below.

In spite of its simplicity, the spontaneous curvature model provides a reliable description for the polymorphism of giant vesicles provided the vesicle membrane contains (at least) one lipid component that undergoes frequent flip-flops between the two bilayer leaflets. In the absence of membrane proteins that act as lipid pumps, lipid flip-flops represent a thermally activated process with flip-flop times that vary from hours or even days for phospholipids<sup>[61–63]</sup> to seconds<sup>[64,65]</sup> or even milliseconds<sup>[66]</sup> for cholesterol and other sterols. In cellular membranes, lipid flip-flops are also induced by proteins, some of which act as lipid pumps.<sup>[67–70]</sup>

The applicability of the spontaneous curvature model to lipid bilayers with cholesterol has been recently demonstrated for two specific lipid mixtures, for a binary mixture of POPC and cholesterol<sup>[28]</sup> as well as for a ternary mixture of POPC, POPG, and cholesterol.<sup>[29]</sup> On the other hand, in the absence of flip-flops, the number of lipids is conserved in each bilayer leaflet separately, which implies that the area difference between the two leaflets has a preferred value. This additional constraint defines the area–difference–elasticity model.<sup>[58,71,72]</sup> The first variation of the ADE model leads to the same stationary shapes as the spontaneous curvature model but the relative stability of these shapes may be different. The difference in the energy landscapes of the two models has been recently studied for the active shape oscillations of giant vesicles as displayed in Figure 5.<sup>[39]</sup>

### 3.1.3. Total Elastic Energy

In the absence of topological transformations, the total elastic energy of a fluid membrane is obtained by adding up the stretching and bending energies. For an arbitrary membrane shape  $S$ , we then obtain

$$E_{el}\{S\} = E_{st}\{S\} + E_{be}\{S\} \quad (5)$$

with the stretching and bending energies as given by Equations (2) and (4), respectively. It turns out that the first variation of the total elastic energy  $E_{el}$  in Equation (5) leads to the same stationary shapes as the first variation of the elastic energy<sup>[73]</sup>

$$E'_{el}\{S\} = \Sigma A\{S\} + E_{be}\{S\} \quad (6)$$

where the stretching energy  $E_{st}$  has been replaced by the term  $\Sigma A$ , that is, by the product of mechanical tension and membrane area. In addition, the tension  $\Sigma$  now plays the role of a Lagrange multiplier that is used to ensure that the membrane area  $A$  has a certain prescribed value.<sup>[60,74]</sup> The formal equivalence of the two elastic energies  $E_{el}\{S\}$  and  $E'_{el}\{S\}$  is not obvious and requires some careful theoretical considerations. Furthermore, strong stretching of the membrane acts to reduce the membrane thickness which will change the curvature-elastic parameters  $\kappa$  and  $m$  as well.

### 3.1.4. Key Parameters of Membrane Shape

In the last paragraphs, we have encountered three elastic parameters: the area compressibility modulus  $K_A$ , the bending rigidity  $\kappa$ , and the spontaneous curvature  $m$ . In addition, we also saw that the membrane area  $A$ , which is a geometric quantity, and its optimal value  $A_0$ , corresponding to a tensionless membrane, play an important role. In fact, for the shape of giant vesicles, we can ignore the area compressibility  $K_A$  and the optimal area  $A_0$ , when we consider the membrane  $A$  as a control parameter that can be directly measured by optical microscopy.<sup>[73]</sup>

Another geometric quantity which is relevant for the shape of vesicles and closed membrane compartments is the volume  $V$  of these compartments. As a consequence, we conclude that the shape of large membrane compartments is determined by two geometric parameter, membrane area  $A$  and vesicle volume  $V$ , as well as by two fluid-elastic parameters, the bending rigidity  $\kappa$  and the spontaneous curvature  $m$ .

The parameters  $A$  and  $\kappa$  have the physical units of length squared and of energy. Thus, we will take the vesicle size  $R_{ve} = \sqrt{A/(4\pi)}$  to be the basic length scale and to measure all lengths in units of  $R_{ve}$ . Note that the vesicle size  $R_{ve}$  is equal to the radius of a spherical vesicle with area  $A$ . Likewise, we will take the bending rigidity  $\kappa$  to be the basic energy scale and measure all energies and free energies in units of  $\kappa$ . As a consequence, we are left with only two rescaled and dimensionless shape parameters which are proportional to the spontaneous curvature and to the vesicle volume. The precise definition of these two shape parameters is provided further

below. In the context of engineering, this reduction of the number of independent parameters by rescaling is known as dimensional analysis.

### 3.2. Local Curvature Generation at the Nanoscale

The spontaneous or preferred curvature of the membrane arises from the transbilayer asymmetry of the two bilayer leaflets. Such an asymmetry can be generated by many different molecular and supramolecular mechanisms. Some of these mechanisms are displayed in **Figure 9**. It is important to note that the lipid bilayers of cellular membranes are asymmetric as well, displaying different lipid compositions in their two leaflets.<sup>[70,75–77]</sup>

#### 3.2.1. Transbilayer Asymmetry of Leaflet Compositions

One simple and general mechanism which should also be relevant for cellular membranes is the compositional asymmetry between the two leaflets, as illustrated in Figure 9a. In the latter panel, the inner (lower) leaflet contains more lipids with large head groups. Such a situation has been studied for GUV membranes that were doped with the glycolipid (or ganglioside) GM1.<sup>[78,79]</sup> The glycolipid GM1 has attracted much recent interest because it is abundant in all mammalian neurons<sup>[80]</sup> and plays an important role in many neuronal processes and diseases.<sup>[81]</sup> Furthermore, GM1 acts as a membrane anchor for various toxins, bacteria, and viruses such as

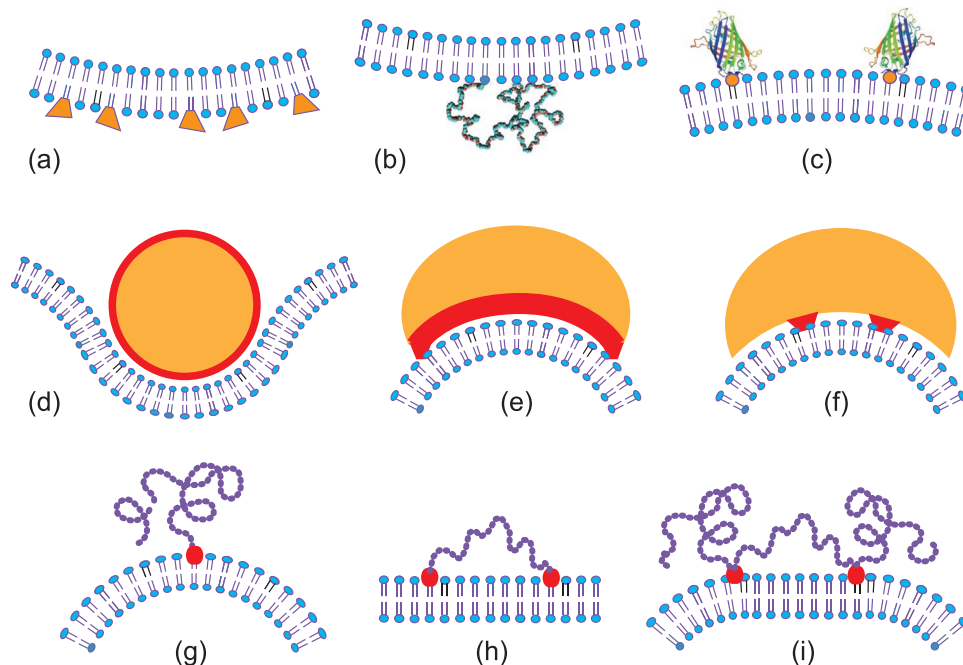


**Figure 9.** Local curvature generation of bilayer membranes via transbilayer asymmetry and spontaneous curvature: a–c) Compositional asymmetry between the two leaflets of the bilayer membranes arising from small molecules, the size of which is smaller or comparable to the bilayer thickness;<sup>[28,29,83]</sup> d–f) Scaffolding based on adhesive colloids and nanoparticles with at least one linear dimension that exceeds the bilayer thickness; and g–i) Entropic scaffolding by flexible molecules anchored to the membranes.<sup>[85–87]</sup> In all panels, the exterior and interior buffer solutions are taken to be above and below the lipid bilayers, respectively. The transbilayer asymmetry and scaffolding then leads to a preferred or spontaneous curvature that is negative in panels (a,b,d) and positive otherwise.

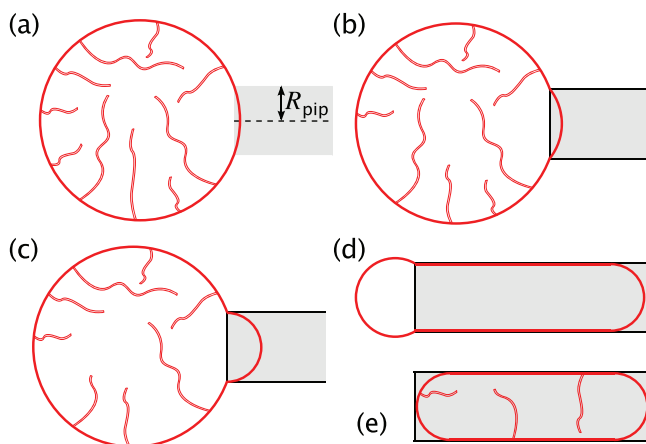


**Figure 10.** Aspiration of tubulated GUV (red) by a micropipette (grey) of radius  $R_{\text{pip}}$ : a) The spherical mother vesicle comes into contact with the pipette; b) With increasing suction pressure, some of the nanotubes are retracted and the mother vesicle develops a tongue that has the form of a spherical cap; c) When the suction pressure reaches a critical value, the cap-like tongue becomes a hemisphere with radius  $R_{\text{pip}}$ , and the vesicle membrane starts to flow into the micropipette; and (d,e) Depending on the membrane area stored in the nanotubes, d) the vesicle motion stops as soon as all nanotubes have been retracted or e) continues until the vesicle is completely aspirated into the pipette. Reproduced under terms of the CC-BY license.<sup>[78]</sup> Copyright 2018, The Authors, published by American Chemical Society.

the simian virus 40.<sup>[82]</sup> The spontaneous curvature induced by the transbilayer asymmetry of GM1 in the GUV membranes was quite large and led to the formation of nanotubes when the GUVs were deflated osmotically. Furthermore, the retraction of the nanotubes by micropipette aspiration was used to measure the spontaneous tension of the membranes,<sup>[78]</sup> as discussed further below, see **Figure 10**. The spontaneous curvature values deduced from the micropipette experiments were  $m = -1/(155 \text{ nm})$  for 2 mol% GM1 and  $m = -1/(95 \text{ nm})$  for 4 mol% GM1. The negative values of the spontaneous curvature  $m$  imply that the nanotubes pointed toward the vesicle interior.

Alternatively, we may think about the adsorption of small solutes such as glucose and sucrose, which were observed to generate the multispherical shapes in **Figure 6**.<sup>[28]</sup> Likewise, compositional asymmetry can also be generated by the adsorption of synthetic polymers such as PEG<sup>[83]</sup> and by the binding of His-tagged proteins such as GFP<sup>[29]</sup> to the membrane. The latter mechanism has been used to control the bud size in **Figure 3** and will be further discussed in the context of neck cleavage and vesicle division.

The previous examples involve small molecules, the size of which is smaller than or comparable to the bilayer thickness of 4–5 nm. A somewhat different mechanism for the generation of local curvature is obtained for larger colloids that are bound to the membrane and act as scaffolds for this membrane. Examples for such colloids include rigid nanoparticles, liquid droplets, and long chain molecules. In order to act as scaffolds, these colloids must have two properties. First, they must have at least one linear dimension that is large compared to the bilayer thickness. Second, they must adhere to the membrane or must be anchored to it.

### 3.2.2. Membrane Scaffolding by Adhesive Nanoparticles

The panels (d–f) of **Figure 9** illustrate the local generation of curvature via the scaffolding of membranes by adhesive nanoparticles. The simplest example for membrane scaffolding is presumably provided by a rigid nanoparticle with a spherical shape as depicted in **Figure 9d**. In this example, the radius of the nanoparticle is about 2.5 times the thickness of the bilayer and the particle is partially engulfed by the membrane. Partial engulfment is stable if the spontaneous curvature of the membrane is opposite to the curvature of the particle-bound membrane segment.<sup>[84]</sup> In general, a nanoparticle can have many different shapes with different patterns of adhesive surface domains. Two such patterns are displayed in **Figure 9e,f**. In **Figure 9e**, the whole concave surface domain is adhesive (red), which implies curvature generation after adhesion (induced fit). In **Figure 9f**, the adhesive surface domains (red) are buried inside the concave part of the particle surface, and the membrane must first bend before it can bind to the particle (conformational selection).

### 3.2.3. Entropic Scaffolding by Flexible Chain Molecules

The scaffolding by rigid nanoparticles arises from the adhesion between the nanoparticles and the membrane. In contrast, the scaffolding by flexible chain molecules is caused by the loss of configurational entropy of the chains resulting from the steric hindrance of chains by the membrane.<sup>[85–87]</sup> In order to stay close to the membrane, the chain molecule must, however, be anchored to the membrane. Several cases for this anchorage of a linear chain molecule need to be distinguished, see **Figure 9g–i**.

The simplest case is provided by a linear chain with a single anchor at one end as depicted in **Figure 9g**. In this case, the membrane bends away from the anchored chain in order to increase the spatial region that is accessible to the other end of the chain.<sup>[85,87]</sup> On the other hand, if we anchor this other chain end to the membrane as well, see **Figure 9h**, the membrane remains essentially flat because the entropic scaffolding is now limited to chain configurations, for which both anchors are close together, whereas large anchor–anchor separations stretch the chain molecule and curve the membrane in the opposite direction.<sup>[86]</sup> In other words, the membrane bulges toward the anchored chain for small anchor–anchor separations and away from this chain for large anchor–anchor separations. These two effects cancel exactly for an ideal chain, that is, when we ignore the chain's self-avoidance, which implies that the chain-induced curvature vanishes.<sup>[86]</sup>

For a chain with two intermediate anchors as in **Figure 9i**, the segment of the chain molecule between these two anchors has the same configurational entropy as the chain with two anchored ends, displayed in **Figure 9h**. Therefore, the chain segment between the two anchors will not bend the membrane adjacent to it. The two dangling end segments, on the other hand, will bend the membrane because each of these end segments can essentially explore the same chain configurations as the linear chain in **Figure 9g**, which is anchored only at one end.

### 3.3. Composite Nature of Membrane Tension

A particularly intriguing and confusing aspect of membrane remodeling is the role of membrane tension. For a bilayer membrane, this tension can be decomposed into two contributions, the mechanical tension  $\Sigma$ , that acts to stretch or compress the membrane as in Equation (1), and the spontaneous tension which is equal to  $2\kappa m^2$  and represents the basic tension scale of curvature elasticity.<sup>[88,89]</sup> Furthermore, the mechanical tension within a bilayer membrane can be divided up into two leaflet tensions that act within the individual leaflets of the bilayer.<sup>[89–91]</sup> In mechanical equilibrium, each of these leaflet tensions must be laterally uniform because each leaflet represents a 2D liquid. In the following, we will discuss these different aspects of membrane tension in some detail.

#### 3.3.1. Mechanical versus Spontaneous Tension

In the framework of curvature elasticity, the shape of a membrane is governed by the first variation of the elastic energy in Equation (6), supplemented by the term  $\Delta PV$ , where  $\Delta P = P_{in} - P_{ex}$  is the pressure difference between the interior and exterior solution and  $V$  is the volume of the vesicle. As a result, one obtains a local shape equation which has the form [58,89]

$$\Delta P \approx 2\Sigma_{tot}M \quad \text{with} \quad \Sigma_{tot} \equiv \Sigma + 2\kappa m^2 \quad (7)$$

up to first order in the mean curvature  $M$ , where  $\Sigma_{tot}$  represents the total membrane tension. The latter tension differs from the mechanical tension  $\Sigma$  by the additional term  $2\kappa m^2 \equiv \sigma$ , the spontaneous membrane tension.<sup>[78,88]</sup> The latter tension is a material parameter that does not depend on the shape of the membrane, in close analogy to the interfacial tension of a liquid droplet.

For a giant mother vesicle that forms long membrane nanotubes, the mechanical tension is small compared to the spontaneous tension and the total membrane tension is dominated by the latter tension. If the mother vesicle has a spherical shape with radius  $R_{mv}$  and the tubes are cylindrical with radius  $R_{cy}$ , the relation between the mechanical tension  $\Sigma$  and the spontaneous tension  $\sigma$  has the form [88]

$$\Sigma \approx \pm \frac{R_{cy}}{R_{mv}} \sigma \quad \text{for small } R_{cy}/R_{mv} \quad (8)$$

This small magnitude of the mechanical tension reflects the large reservoirs of membrane area provided by the nanotubes. Indeed, when the tubulated vesicle is exposed to external forces or constraints, it can adapt to these perturbations, for fixed vesicle volume and membrane area, by simply shortening the nanotubes.

This increased robustness of tubulated vesicles has been demonstrated by micropipette aspiration of giant vesicles with inward-pointing nanotubes, as displayed in Figure 10.<sup>[78]</sup> As shown in this figure, the tubules were pointing toward the interior of the vesicle, which provides direct evidence for a

large negative spontaneous curvature of the membrane. In this case, the negative spontaneous curvature was generated by the glycolipid (or ganglioside) GM1 that was enriched in the inner leaflet of the bilayer, see Figure 9a. The micropipette experiments confirmed that the spontaneous tension is a material parameter which plays the same role for tubulated giant vesicles as the interfacial tension for liquid droplets. Indeed, if the area reservoir provided by the membrane nanotubes is sufficiently large, the micropipette aspiration of the vesicles leads to a mechanical instability and to the uptake of the vesicle by the micropipette, as in Figure 10e, in close analogy to the corresponding mechanical instability that has been observed during the micropipette aspiration of a liquid droplet.<sup>[92–94]</sup>

#### 3.3.2. Spontaneous Curvature and Spontaneous Tension

A simple and intuitive understanding of the spontaneous tension can be obtained as follows. Consider a giant vesicle that has a spherical shape because of osmotic inflation, even though its membrane has a large spontaneous curvature  $m$ . In this situation, the bending energy in Equation (4) becomes equal to  $E_{be} \approx 2\kappa m^2 A = \sigma A$  which reveals that the spontaneous tension  $\sigma = 2\kappa m^2$  represents the intrinsic tension scale of curvature elasticity.<sup>[88]</sup> This tension is proportional to the square of the spontaneous curvature  $m$  and thus becomes large for large positive and large negative values of  $m$ .

For giant vesicles, large spontaneous curvatures can be detected by osmotic deflation and the subsequent formation of small buds and/or thin nanotubes. Large positive and negative spontaneous curvatures lead to buds and tubes that protrude into the exterior and interior solution, respectively. This method has been used for a variety of systems in which the giant vesicles responded to different molecules as summarized in Table 1. The observed budding and tubulation processes have been analyzed using the theory of membrane elasticity which led to the values for the spontaneous curvature  $m$  and spontaneous tension  $\sigma$  as displayed in the table. Table 1 also provides those estimates for the bending rigidity  $\kappa$  that were used to compute the spontaneous tension.

The first two columns in Table 1 were obtained for giant vesicles exposed to two aqueous phases of PEG-dextran solutions. The vesicle membranes were composed of dioleoylphosphatidylcholine (DOPC), dipalmitoylphosphatidylcholine (DPPC), and cholesterol. Based on the ternary phase diagrams

**Table 1.** Spontaneous curvature  $m$ , bending rigidity  $\kappa$ , and spontaneous tension  $\sigma = 2\kappa m^2$  for giant vesicles that undergo budding and tubulation in response to a variety of molecular interactions, see the main text.

	PEG-dextran, Lo phase <sup>[83]</sup>	PEG-dextran, Ld phase <sup>[83]</sup>	GM1, 2 mol% <sup>[78]</sup>	GM1, 4 mol% <sup>[78]</sup>	Glucose– sucrose, asymmetry I <sup>[28]</sup>
$m$ [ $\mu\text{m}^{-1}$ ]	$-(1.6 \pm 0.2)$	$-(8 \pm 2)$	$-(6.45 \pm 1.3)$	$-(10 \pm 2)$	$1.3 \pm 1$
$\kappa$ [ $10^{-19}$ J]	3.6	0.8	$\approx 1$	$\approx 1$	$\approx 1$
$\sigma$ [ $\text{mN m}^{-1}$ ]	$1.8 \times 10^{-3}$	$1.02 \times 10^{-2}$	$8.3 \times 10^{-3}$	$2.2 \times 10^{-2}$	$3.4 \times 10^{-4}$

elucidated in refs. [31,95,96], two specific lipid compositions were studied that form a liquid-ordered (Lo) and a liquid-disordered (Ld) phase, corresponding to the two end points of a certain tie line in the phase diagram. The third and fourth columns in Table 1 describe the results for vesicle membranes that were prepared with different mole fractions of the glycolipid (or ganglioside) GM1. The rightmost column in Table 1 corresponds to the transbilayer asymmetry generated by an interior sucrose solution and an exterior glucose solution, which was observed to generate many different multispherical shapes, see Figure 6.

Recently, an unprecedented control over the spontaneous curvature has been achieved by binding His-tagged proteins to the outer leaflets of giant vesicles.<sup>[29]</sup> The vesicle membranes were doped with certain anchor lipids. For His-tagged GFP and 1 mol% anchor lipids, the spontaneous curvature  $m$  was found to increase linearly with the molar solution concentration  $X$  of the protein according to<sup>[29]</sup>

$$m = \frac{1.86}{\mu\text{m}} \frac{X}{nM} \quad \text{for } 0 < X \leq 24 \text{ nM} \quad (9)$$

Thus, if the giant vesicle is exposed to His-tagged GFP at a molar concentration of 24 nM, the spontaneous curvature becomes  $m = 44.6 \mu\text{m}^{-1}$ , a surprisingly large value. The bending rigidity was estimated to be  $48 k_B T$  or  $2.4 \times 10^{-19}$  J which implies that the spontaneous tension  $\sigma$  reached the value  $0.96 \text{ mN m}^{-1}$  for the molar concentration  $X = 24 \text{ nM}$ . Thus, the spontaneous tension varies from  $10^{-4} \text{ mN m}^{-1}$  for asymmetric solutions of simple sugars, see rightmost column of Table 1 up to about  $1 \text{ mN m}^{-1}$  for membranes exposed to His-tagged GFP in the exterior solution at a concentration of 24 nM.

The coverage of the membrane by His-tagged GFP, that is, the density of the membrane-bound GFP has been estimated by calibrating the fluorescence signal of GFP with the corresponding signal of another lipid-dye similar to GFP. One then finds that the average separation of the lipid-anchored GFPs always exceeded 24 nm, which is much larger than GFP's lateral size of about 3 nm.<sup>[97]</sup> Therefore, the surprisingly large spontaneous curvature  $m$  as described by Equation (9) corresponds to a rather low density of membrane-bound GFP. A similar behavior has been found for the large spontaneous curvature generated by a low density of membrane-bound amphiphysin.<sup>[98]</sup>

### 3.3.3. Mechanical Membrane Tension

The previous discussion of the membrane's elastic energies implies that the mechanical tension can be theoretically described in two apparently distinct but nevertheless equivalent ways. The most intuitive description is provided by Equation (1) which relates the mechanical tension  $\Sigma$  to the area dilation  $(A - A_0)/A_0$  of a membrane segment where  $A_0$  represents the area of the tensionless segment. Positive and negative area dilations correspond to stretching and compression of the membrane segment. The corresponding stretching energy  $E_{st}$  is given by Equation (2) and the total elastic energy is then obtained from the superposition of this stretching energy with

the bending energy  $E_{be}$  as in Equation (5). Alternatively, one may use the mechanical tension  $\Sigma$  as a Lagrange multiplier and consider the first variation of the bending energy under the constraint that the membrane area is equal to  $A$ , see Equation (6).

In equilibrium, the mechanical tension must be uniform along the whole membrane. Indeed, if the tension varied along the membrane, the resulting tension gradient would generate lipid flow toward the larger tension until the tension reaches a uniform value. In contrast to the spontaneous tension, the mechanical tension depends on the size and shape of a membrane as will be shown explicitly for multispherical vesicles, for which the mechanical tension depends on the curvature-elastic parameters  $\kappa$  and  $m$  and, in addition, on the volume  $v$ .

### 3.4. Leaflet Tensions of Bilayer Membranes

The mechanical tension discussed so far represents the tension experienced by the whole bilayer membrane. Lipid bilayers consist of two leaflets which are kept in close contact via the hydrophobic effect. If we monitored the movements of individual lipid molecules, we would see that each molecule stays in its leaflet for an extended period of time until it undergoes a transbilayer flip-flop from one leaflet to the other one. In the absence of membrane proteins that act as lipid pumps, the flip-flops represent a thermally activated process with flip-flop times that vary from hours or even days for phospholipids<sup>[61–63]</sup> to seconds<sup>[64,65]</sup> or even milliseconds<sup>[66]</sup> for cholesterol and other sterols. In cellular membranes, lipid flip-flops are also induced by proteins, some of which act as lipid pumps.<sup>[67–70]</sup>

Each leaflet represents a separate 2D liquid. In mechanical equilibrium, each leaflet is then characterized by a certain uniform leaflet tension. If we denote these two tensions by  $\Sigma_{l1}$  and  $\Sigma_{l2}$ , the mechanical bilayer tension  $\Sigma$  becomes equal to the sum of the two leaflet tensions, that is,<sup>[16,90,91,99]</sup>

$$\Sigma = \Sigma_{l1} + \Sigma_{l2} \quad (10)$$

One direct and important consequence of this relation is that tensionless bilayers with  $\Sigma = 0$  may still have significant leaflet tensions with  $\Sigma_{l2} = -\Sigma_{l1}$ . Therefore, if leaflet 1 is stretched with  $\Sigma_{l1} > 0$ , leaflet 2 is compressed with  $\Sigma_{l2} < 0$ , and vice versa.

#### 3.4.1. Leaflet Tensions from Molecular Simulations

In molecular simulations, the mechanical tension is obtained from the stress (or pressure) profile across the bilayer. This stress profile can be decomposed into two contributions from the individual leaflets after we have determined the molecular interface between these two leaflets. Because of thermal noise, this interface is rough and we need to consider certain procedures to define the average position of the interface, which we call the “midsurface.” Several computational procedures have been used to obtain this midsurface.<sup>[16,91,99]</sup> All of these procedures have been found to give rather similar results. The presumably simplest procedure is to define the midsurface via the density profile of the hydrophobic core of the bilayer membrane. In contrast to the neutral surface of a bilayer,<sup>[100,101]</sup> the

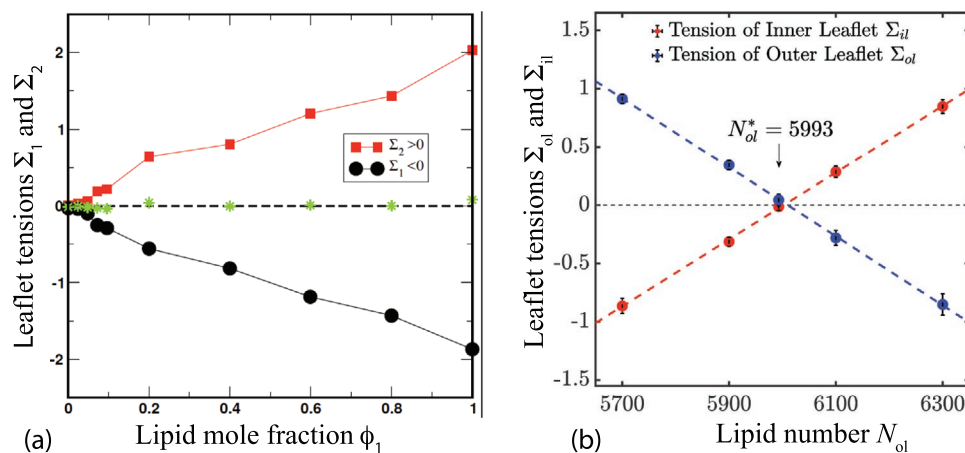


**Figure 11.** Leaflet tensions of tensionless bilayers without flip-flops: a) Leaflet tensions  $\Sigma_1$  and  $\Sigma_2$  of planar and tensionless bilayers with two lipid components, LH and SH.<sup>[91]</sup> The tensions are plotted against the mole fraction  $\phi_1$  of the LH component in leaflet 1 and no LH lipids in leaflet 2; and b) Leaflet tensions  $\Sigma_{oi}$  and  $\Sigma_{ii}$  of the outer and inner leaflets of spherical nanovesicles.<sup>[6]</sup> The tensions are plotted against the number  $N_{oi}$  of lipids in the outer leaflet. The lipid number  $N_{oi}$  was varied by reshuffling the lipids between the two leaflets for fixed total number of lipids in the two leaflets. Both leaflet tensions vanish simultaneously for a) zero  $\phi_1$  and b) for  $N_{oi} = 5993$ . (a) Reproduced under terms of the CC-BY license.<sup>[91]</sup> Copyright 2018, The Authors, published by AIP Publishing LLC. (b) Reproduced with permission.<sup>[6]</sup> Copyright 2019, American Chemical Society.

midsurface considered here is not defined in terms of elastic deformations or stresses.

Two examples for the leaflet tensions of tensionless bilayers are displayed in **Figure 11**. In panel (a) of this figure, we see a plot of the two leaflet tensions for planar and tensionless bilayers. These bilayers contained two lipid components that differed in the size of their head groups. The leaflet tensions were changed by varying the mole fraction  $\phi_1$  of the lipids with the larger head groups in leaflet 1. In panel (b) of Figure 11, we see a similar plot for the two leaflet tensions of spherical nanovesicles. In this case, we controlled the leaflet tensions by reshuffling lipid molecules from one leaflet to another. Thus, we considered a fixed total number of lipids,  $N_{oi} + N_{ii}$ , and varied the number  $N_{oi}$  in the outer leaflet by redistributing the lipids between the two leaflets.

One important function of intracellular membranes is to provide different spatial compartments with a strictly controlled exchange of molecules between these compartments. In order to provide a large barrier for diffusive transport, biomembranes usually have a relatively low bilayer tension. However, even if the bilayer tension is close to zero, the leaflet tensions can still have a rather large magnitude as shown in Figure 11. In this figure, the leaflet tensions are displayed in units of  $k_B T/d^2$  which is equal to  $5 \text{ mN m}^{-2}$ . For comparison, a bilayer tension of such a magnitude is likely to rupture the membrane.

### 3.4.2. Relaxation of Leaflet Tensions by Flip-Flops

The data in Figure 11 were obtained from simulations over tens of microseconds. On these time scales, the lipids did not undergo transbilayer flip-flops from one leaflet to the other. Therefore, the numbers of lipids that were initially assembled in the two leaflets did not change during the simulations. Now, let us add another lipid species such as cholesterol that undergoes frequent flip-flops even on the time scales of the simulations. The obvious question now is: how do the leaflet tensions behave in the presence of such flip-flops. In order to

address this question, we studied the planar bilayers depicted in **Figure 12**.<sup>[99]</sup>

As shown in the top row of this figure, we first looked at a tensionless bilayer with two lipid components and focussed on the situation in which the upper leaflet was compressed and the lower leaflet was stretched, corresponding to the upper leaflet tension  $\Sigma_{i1} < 0$  and the lower leaflet tension  $\Sigma_{i2} > 0$  that add up to zero. We then added a certain number of cholesterol to this bilayer which we distributed symmetrically between the two leaflets. Intuitively, one would expect that a cholesterol molecule that dwells in the compressed leaflet is more likely to undergo a flip-flop compared to a cholesterol that dwells in the stretched leaflet. Therefore, for long times, the average number of cholesterols in the lower leaflet should be larger than the average number of cholesterols in the upper leaflet. Such a biased distribution was indeed observed. At the same time, the leaflet tensions relaxed to zero with a characteristic decay time of about 55 ns. A different behavior has been observed in simulations of mixed lipid bilayers with two phospholipids and cholesterol.<sup>[102]</sup> In the latter case, the bilayer was reported to relax toward a state with two finite leaflet tensions of about  $\pm 3.7 \text{ mN m}^{-2}$ . These leaflet tensions are quite large and can lead to an instability of the bilayer membrane.

### 3.4.3. Leaflet Tensions and Bilayer Curvature

Finite leaflet tensions of tensionless bilayers provide an intuitive understanding for the generation of spontaneous curvature. Thus, if leaflet 1 is compressed and leaflet 2 is stretched, both leaflets can reduce their stress by curving in such a way that the area of leaflet 1 is increased and the area of leaflet 2 is decreased. Thus, if leaflet 1 is in contact with the exterior solution, the bilayer should attain a positive spontaneous curvature and bulge toward the exterior solution. Alternatively, when we think of the two water–lipid interfaces, the interface of the stretched leaflet with the aqueous solution should have a larger interfacial tension than the interface of the compressed leaflet. The bilayer should then attain a positive spontaneous

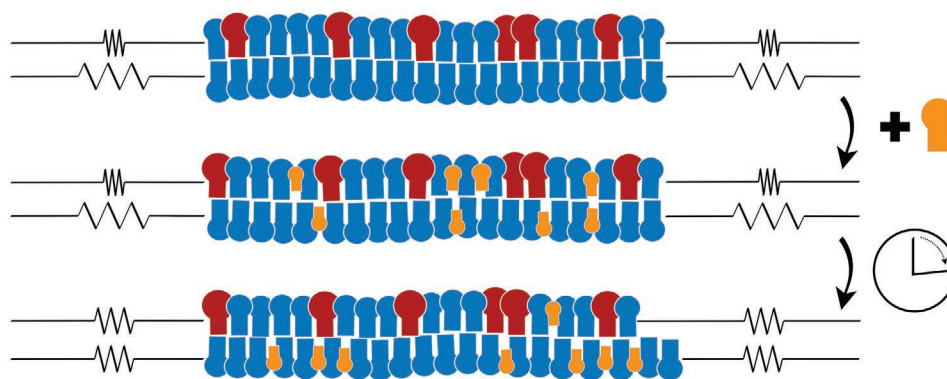


**Figure 12.** Relaxation of leaflet tensions in the presence of flip-flops: The top row shows a bilayer membrane with two lipid components (blue and red) that do not undergo flip-flops from one leaflet to the other. The bilayer tension  $\Sigma = \Sigma_1 + \Sigma_2$  is (close to) zero. However, the upper leaflet of the bilayer is compressed by a negative leaflet tension  $\Sigma_1 < 0$  whereas the lower leaflet is stretched by a positive leaflet tension  $\Sigma_2 > 0$ , as indicated by the schematic springs acting on the bilayer edges. As a third component, cholesterol (orange) is added to both leaflets so that they initially contain the same number of cholesterol molecules, as depicted in the middle row. During the subsequent relaxation process, the cholesterol transbilayer distribution becomes asymmetric with a larger number of cholesterols in the lower leaflet. Furthermore, both leaflets relax toward a tensionless state as indicated by the relaxed springs. The cartoon at the bottom also indicates that the two tensionless leaflets typically differ in their preferred areas. Reproduced under terms of the CC-BY license.<sup>[99]</sup> Copyright 2019, The Authors, published by American Chemical Society.

curvature in order to reduce the interfacial free energy of the two water–lipid interfaces.<sup>[90]</sup> The latter view was expressed a long time ago in the context of asymmetric monolayers.<sup>[103,104]</sup>

However, even tensionless leaflets may generate a significant spontaneous curvature as has been observed for the bilayer system displayed in the bottom row of Figure 12.<sup>[99]</sup> This asymmetry can be understood from the analysis of the underlying stress profile. A tensionless bilayer implies that the  $z$ -integral over this profile must vanish, where  $z$  is the coordinate perpendicular to the midplane of the bilayer. In addition, in order to compute the leaflet tensions, we need to divide the stress profile up into two leaflet contributions. Vanishing leaflet tensions imply that the  $z$ -integrals over each leaflet contribution vanish separately. However, even in the latter situation, the total stress profile may be asymmetric and generate a significant spontaneous curvature.<sup>[99]</sup>

## 4. Local Properties of Membrane Necks

In this section, we will first emphasize the different views of membrane necks at the nanoscale and at the micron scale. These two views differ in their resolution: on the nanoscale, the finite thickness of the bilayer membrane plays a significant role whereas this thickness can be ignored at the micron scale, because of the large separation of length scales between the bilayer thickness and the lateral size of the membrane. On the micron scale, closed membrane necks can be characterized by several local properties: by a neck curvature that depends on the mean curvatures of the two membrane segments adjacent to the neck; a condition for the stability of closed necks; and a curvature-dependent constriction force acting on the neck.

### 4.1. Different Views of Membrane Necks

Closed membrane necks look quite different when we view them with nanoscale and with micron scale resolution. These

two different views are displayed in **Figure 13**. In panels (a) and (b) of this figure, we see a closed membrane neck at the nanoscale, as observed in molecular dynamics simulations. The lipid bilayer has a thickness of about 4 nm and forms a neck with an hourglass-like shape. The neck is axisymmetric and has a circular waistline. For a closed neck, the outer radius of this waistline is equal to twice the bilayer thickness whereas the inner radius vanishes. For the examples shown in Figure 13a,b, the vesicle size is about 36 nm, which is the radius of the spherical vesicles that we would obtain from the dumbbell-shaped vesicles by osmotic inflation. Inspection of the simulation snapshots shows that the hourglass-shaped neck is highly curved in the sense that its contour curvature is large.

At the micron scale, the view of the membrane neck as obtained by optical microscopy is quite different, see panels (c) and (d) in Figure 13. Indeed, when viewed with optical microscopy, the hourglass-shaped membrane segment is no longer visible but is replaced by the touching point of the two spheres connected by the neck. Thus, one might view the point-like neck as a direct consequence of the limited optical resolution. It turns out, however, that this point-like neck correctly captures two important aspects of the neck. First, during neck closure, the principal curvatures diverge but the mean curvature attains a finite limit. Second, this mean curvature of the neck is directly related to the curvature radii of the two adjacent membrane segments which one can read off from the optical images.

#### 4.1.1. Closure of Hourglass-Shaped Neck

We will now discuss the closure of the hourglass shape in more detail. In Figure 13a, the waistline (wl) of the hourglass-shaped neck forms a circle with radius  $R_{ne}$ . Along this waistline, the neck is characterized by two principal curvatures, the negative contour curvature  $C_{1,wl} < 0$  perpendicular to the waistline and the positive principal curvature  $C_{2,wl} = 1/R_{ne} > 0$  parallel to the waistline. When the neck closes, the neck radius goes to zero and the principal curvature  $C_{2,wl}$  diverges. However, the mean curvature

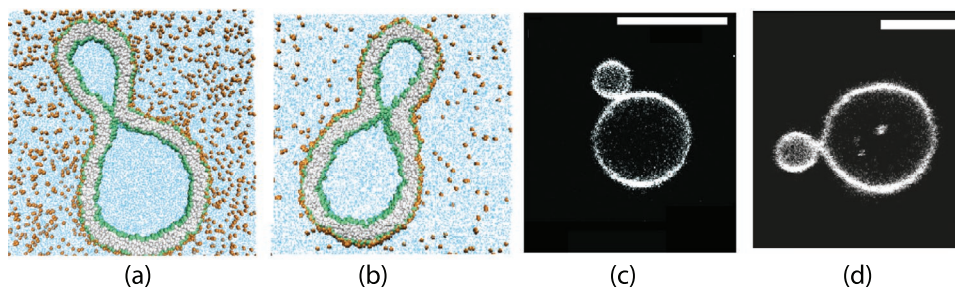


**Figure 13.** Closed membrane necks viewed on nano and micron scales: a,b) Two examples for the hourglass-like shape of closed necks on the nanoscale where we still resolve the molecular bilayer. Both exterior solutions contain small solutes such as simple sugars (orange)<sup>[17]</sup>: a large solute concentration for good solvent conditions in (a) and a small concentrations for poor solvent conditions in (b); and c,d) Optical images of giant vesicles. The scale bar is 10  $\mu\text{m}$  in (c) and 5  $\mu\text{m}$  in (d). Reproduced under terms of the CC-BY license.<sup>[17]</sup> Copyright 2021, The Authors, published by American Chemical Society.

$$M_{\text{wl}} = \frac{1}{2}(C_{1,\text{wl}} + C_{2,\text{wl}}) \quad (11)$$

remains finite and satisfies the asymptotic equality

$$M_{\text{wl}} \approx M_{\text{ne}} \equiv \frac{1}{2}(M_l + M_s) \quad (12)$$

in the limit of small  $R_{\text{ne}}$ <sup>[39]</sup> with the mean curvature  $M_{\text{ne}}$  of the closed neck determined by the mean curvatures  $M_l$  and  $M_s$  of the two membrane segments,  $l$  and  $s$ , adjacent to the neck. Thus, as the neck closes, the positive singular contribution from the second principal curvature  $C_{2,\text{wl}} = 1/R_{\text{ne}} > 0$  is cancelled by another negative contribution arising from the contour curvature  $C_{1,\text{wl}}$ , which corresponds to a singular catenoid. The remaining regular neck curvature  $M_{\text{ne}}$  may be positive or negative depending on the two mean curvatures of the adjacent membrane segments.

#### 4.2. Curvature and Stability of Closed Membrane Necks

In the framework of curvature elasticity, the stability of a closed membrane neck is described by a surprisingly simple relation

which depends only on the spontaneous curvature  $m$  and on the local geometry of the neck. This geometry is provided by the curvatures of the two membrane segments that are joined via the neck and define the corresponding neck curvature  $M_{\text{ne}}$  as in Equation (12). Two cases corresponding to interior and exterior necks must be distinguished as shown in **Figure 14**. The interior neck is formed by an outward-pointing bud whereas the exterior neck is formed by an inward-pointing bud. In order to avoid confusion, we will use the terms “interior” and “exterior necks” rather than “outward” and “inward-pointing buds.”<sup>[105]</sup>

The interior neck in **Figure 14a** connects two interior compartments. Close to the interior neck, the two compartments are in contact with two membrane segments that have a positive mean curvature. In contrast, the exterior neck in **Figure 14b** connects two exterior compartments. Close to the exterior neck, the two compartments are in contact with two nested membrane segments, an outer and an inner one. The outer membrane segment has positive mean curvature, whereas the inner membrane segment has negative mean curvature. Furthermore, all necks that have been explicitly studied within the framework of curvature elasticity have been axisymmetric and had a circular cross-section. Therefore, we will now focus on such axisymmetric necks which implies that the two

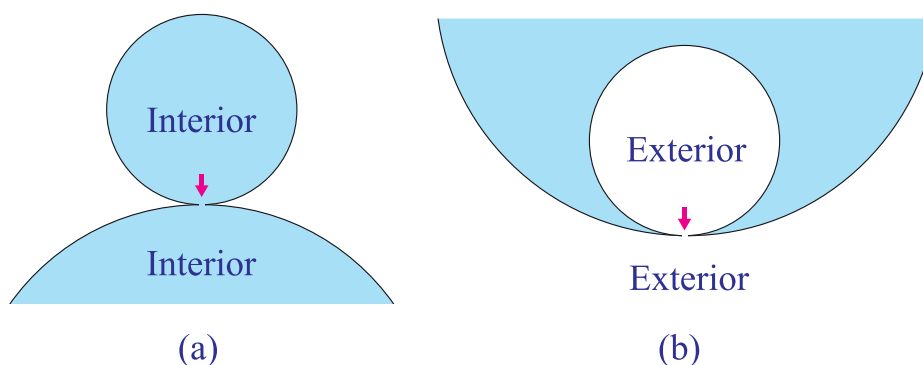


**Figure 14.** Membrane necks or “worm holes” (red arrows) between different membrane compartments: a) Interior neck between two interior compartments (light blue) which is formed by membranes with a positive spontaneous curvature. In this case, both membrane segments adjacent to the neck have positive mean curvatures which implies that the interior neck curvature  $M_{\text{ne}}$  is positive as well; and b) Exterior neck between two exterior compartments (white) which is formed by membranes with a negative spontaneous curvature. Now, the membrane segment in contact with the exterior bulk compartment has positive mean curvature whereas the membrane segment engulfing the small exterior compartment has negative mean curvature, which implies that the exterior neck curvature  $M_{\text{ne}}$  is negative. For a plasma membrane, the interior compartment is the cytosol. For a membrane-bound organelle, the interior compartment is the lumen of the organelle.

adjacent membrane segments can be characterized by their curvature radii close to the neck. These curvature radii will be denoted by  $R_l$  and  $R_s$  where the subscripts “l” and “s” refer to “large” and “small,” respectively, corresponding to the large and small membrane compartments in Figures 14a and 14b.

For an interior neck as in Figure 14a, the neck curvature  $M_{ne}$  is then given by

$$M_{ne} = \frac{1}{2}(M_l + M_s) = \frac{1}{2}\left(\frac{1}{R_l} + \frac{1}{R_s}\right) \quad (\text{interior neck}) \quad (13)$$

which is always positive. For an exterior neck as in Figure 14b, on the other hand, the neck curvature has the form

$$M_{ne} = \frac{1}{2}(M_l + M_s) = \frac{1}{2}\left(\frac{1}{R_l} - \frac{1}{R_s}\right) \quad (\text{exterior neck}) \quad (14)$$

because the mean curvature  $M_s$  is now negative (note that all radii are taken to be positive). The neck curvature of an exterior neck is always negative because the curvature radius  $R_s$  is necessarily smaller than the curvature radius  $R_l$ .

An interior neck as in Figure 14a is stably closed provided the spontaneous curvature  $m$  is positive and sufficiently large. More precisely, the closed interior neck is stable if

$$m \geq M_{ne} = \frac{1}{2}\left(\frac{1}{R_l} + \frac{1}{R_s}\right) \quad (\text{stability of interior neck}) \quad (15)$$

The equality  $m = M_{ne}$  describes the closure of the neck which opens up for  $m < M_{ne}$ . For giant vesicles, the neck curvature can be directly obtained from the microscopy images of the two-sphere vesicles as in Figures 2 and 3, which provides a simple and useful approach to estimate the spontaneous curvature  $m$  experimentally.<sup>[28,29]</sup>

On the other hand, an exterior neck as in Figure 14b is stably closed if the spontaneous curvature is negative with a sufficiently large absolute value  $|m|$ . Indeed, the closed neck condition now has the form

$$m \leq M_{ne} = \frac{1}{2}\left(\frac{1}{R_l} - \frac{1}{R_s}\right) \quad (\text{stability of exterior neck}) \quad (16)$$

Because the neck curvature  $M_{ne}$  is always negative for exterior necks, this inequality can only be fulfilled when the spontaneous curvature  $m$  is negative as well. The equality  $m = M_{ne}$  again describes the closure of the neck which now opens up for  $m > M_{ne}$ .

The stability relations for closed membrane necks can be derived by starting from a dumbbell shape with an open but narrow neck and parameterizing this shape by a piece-wise constant-mean-curvature surface. One such parameterization consists of two hemispheres connected by two unduloid segments that form a narrow neck of radius  $R_{ne}$ .<sup>[106–108]</sup> The dumbbell with a closed neck is obtained in the limit of zero neck radius  $R_{ne}$ . The bending energy  $E_{be}$  of the dumbbell has the form [58, 89]

$$E_{be}(R_{ne}) \approx E_{be}(0) \pm 8\pi\kappa(m - M_{ne})R_{ne} \quad (17)$$

up to first order in  $R_{ne}$  where the plus and minus sign applies to interior and exterior necks, respectively. The closed neck is stable if the term proportional to the neck radius  $R_{ne}$  increases with increasing  $R_{ne}$  which implies  $m > M_{ne} > 0$  for interior necks and  $m < M_{ne} < 0$  for exterior necks.

### 4.3. Curvature-Induced Constriction Forces

The spontaneous curvature generates a constriction force  $f$  at the membrane neck which can be defined via the relation  $f = \partial E_{be}/\partial R_{ne}$ . Using the expression for the bending energy as given by Equation (17), we then obtain the constriction forces<sup>[29,58,89]</sup>

$$f \approx 8\pi\kappa(m - M_{ne}) \quad \text{for interior necks with } m > 0 \quad (18)$$

and

$$f \approx 8\pi\kappa(M_{ne} - m) \quad \text{for exterior necks with } m < 0 \quad (19)$$

up to first order in the neck radius  $R_{ne}$ . If the constriction force  $f$  at the membrane neck is sufficiently large, the neck is cleaved as recently demonstrated for the controlled division of giant vesicles.<sup>[29]</sup> In these experiments, the binding of His-tagged proteins to the outer leaflets of the vesicle membranes was used to fine-tune the spontaneous curvature  $m$  as in Figure 3 and Equation (9). The resulting constriction force  $f$  is displayed in **Figure 15** and can be sufficiently large to divide the vesicles.

If the membrane neck contains a domain boundary between two lipid domains as in Figure 4, the constriction force is enhanced by the line tension  $\lambda$  of this domain boundary. Indeed, one has to take the line energy of the domain boundary into account, which is equal to  $2\pi R_{ne}\lambda$ , which implies the additional contribution  $\Delta f = 2\pi\lambda$  to the constriction force for both interior and exterior necks. This force contribution is always positive and, thus, constrictive because the line tension  $\lambda$  of a domain boundary between two lipid phase domains must be positive as required by thermodynamic stability. This enhancement of the constriction force by a domain boundary facilitates neck fission and vesicle division as has been recently demonstrated experimentally,<sup>[37]</sup> see Figure 4c. A significant constriction force is necessary for membrane fission and vesicle division. In addition, the Gaussian curvature modulus must be negative in order for the fission process to be “downhill” (or exergonic) and, thus, to occur spontaneously, see Section 7.2.

In general, the two lipid domains may differ in their spontaneous curvatures and bending rigidities. Thus, consider two lipid domains,  $a$  and  $b$ , formed by two coexisting lipid phases, which have spontaneous curvatures  $m_a$  and  $m_b$  as well as bending rigidities  $\kappa_a$  and  $\kappa_b$ , respectively. Adjacent to the closed membrane neck, the two domains have the mean curvature  $M_a$  and  $M_b$ . Generalizing the piece-wise constant-mean-curvature parameterization of the dumbbell shape to this case,<sup>[107,108]</sup> the constriction force  $f$  becomes

$$f = 2\pi\lambda \pm 4\pi[\kappa_a(m_a - M_a) + \kappa_b(m_b - M_b)] \quad (20)$$

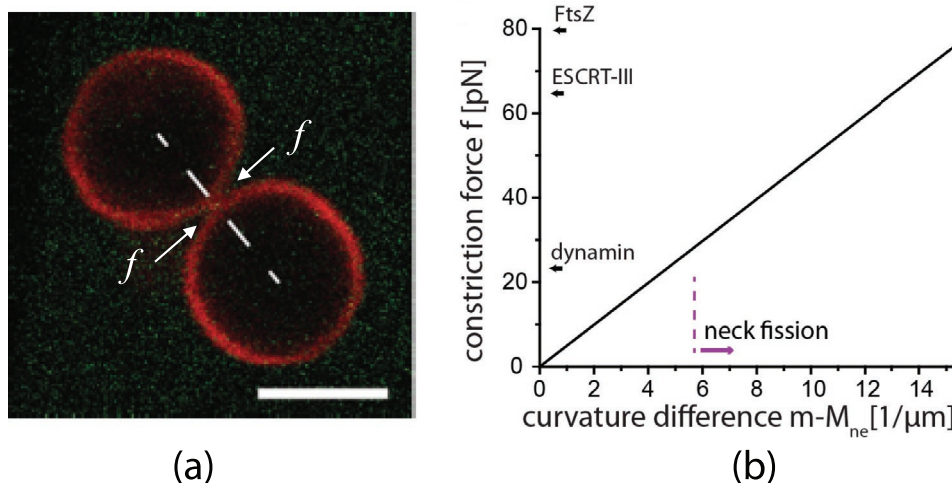


**Figure 15.** Constriction force  $f$  at membrane neck: a) Confocal image of a giant vesicle that consists of two spheres connected by a narrow interior neck. The spontaneous curvature is generated by His-tagged GFP which binds to the membrane from the exterior solution. The constriction force  $f$  (white arrows) acts to compress this neck. The scale bar is  $5 \mu\text{m}$ ; and b) Constriction force  $f$  generated by GFP as a function of the curvature difference  $m - M_{\text{ne}}$ . The straight line corresponds to Equation (18) with  $\kappa = 48 k_B T$ . For comparison, the plot also includes literature values for the constriction forces as generated by the specialized protein complexes of dynamin,<sup>[109]</sup> ESCRT-III,<sup>[110]</sup> and FtsZ<sup>[111]</sup>

where the plus and minus sign again applies to interior and exterior necks. Furthermore, it has been tacitly assumed here that the difference between the Gaussian curvature moduli of the two domains is small and can be ignored. If this difference is significant, the domain boundary is shifted out of the neck.<sup>[107,112]</sup>

Membrane necks are also formed during the engulfment of rigid particles and droplets in aqueous two-phase systems. For the engulfment of rigid particles, both the closed neck condition and the constriction forces involve the adhesive strength between particle and membrane.<sup>[113]</sup> For the engulfment of liquid droplets that partially wet the membrane, the interface between the two aqueous phases can minimize its interfacial free energy by being located in the neck but this free energy is proportional to  $R_{\text{ne}}^2$ . Therefore, for axisymmetric necks as considered here, the closed neck conditions and constriction forces remain unchanged to leading order in  $R_{\text{ne}}$ .<sup>[54]</sup> Neck should be axisymmetric as long as the contact line of the droplet with the membrane has a positive line tension  $\lambda_{\text{co}}$ . However, in contrast to the line tension of domain boundaries, the line tension of contact lines does not have to be positive but can be negative. In fact, the contact line tension  $\lambda_{\text{co}}$  of droplets adhering to lipid bilayers has been found to be negative for a wide range of parameters which leads to a spontaneous symmetry breaking of the rotational symmetry and to a tight-lipped shape of membrane neck and contact line, as shown in Figure 8.<sup>[46]</sup>

## 5. Two-Sphere Vesicles as a Case Study

In this section, we will discuss the properties of two-sphere vesicles which provide the simplest examples for vesicles with closed necks. The following description will be somewhat technical but provides a case study which can be directly generalized to multispheres with more than two spheres connected by more than one closed neck, as discussed in Section 6.

We will distinguish two types of two-sphere vesicles, which are formed for positive and negative spontaneous curvature. For positive spontaneous curvature, the two spheres are joined by interior necks which connect two interior subcompartments of the vesicle. For negative spontaneous curvature, the two spheres are joined by exterior necks which connect two compartments of the exterior solution. In both cases, we consider the vesicle morphologies as a function of two dimensionless shape parameters, the rescaled volume  $\nu$  and the rescaled spontaneous curvature  $\bar{m}$  which define the morphology diagram of the vesicles. The two-sphere vesicles are stable in certain sub-regions of the morphology diagram. These stability regimes are bounded by two lines of limit shapes, denoted by  $L_{1+1}$  and  $L_{2*}$ . Within these regimes, the shape of the two-sphere vesicles depends only on the volume  $\nu$  but not on the spontaneous curvature  $\bar{m}$ . However, both the constriction force acting on the membrane neck and the membrane tensions depend on the spontaneous curvature.

Both shape parameters  $\nu$  and  $\bar{m}$  can be controlled experimentally: the volume  $\nu$  can be varied by the osmotic conditions whereas the spontaneous curvature  $\bar{m}$  can be controlled by a variety of mechanisms as illustrated in Figure 9. A high-precision method to control the spontaneous curvature has been recently introduced based on the binding of His-tagged proteins such as GFP to one leaflet of the vesicle membrane, see Figures 3, 9c, and Figure 15 as well as Equation (9).

### 5.1. Dimensionless Shape Parameters

We will focus on membranes with uniform molecular composition and, thus, uniform elastic properties. As mentioned previously, the shape of such a membrane depends on two fluid-elastic parameters, the bending rigidity  $\kappa$  and the spontaneous curvature  $\bar{m}$ . The bending rigidity has the units of energy, which will be used as the basic energy scale.

Consider a vesicle with surface area  $A$  and volume  $V$ . Define the vesicle size  $R_{ve}$  via

$$R_{ve} \equiv \sqrt{A/(4\pi)} \quad (21)$$

and the rescaled volume or volume-to-area ratio by

$$\nu \equiv \frac{V}{\frac{4\pi}{3} R_{ve}^3} \quad \text{with } 0 < \nu \leq 1 \quad (22)$$

We will also use the dimensionless spontaneous curvature

$$\bar{m} \equiv mR_{ve} \quad (23)$$

In general, the vesicle shapes which minimize the elastic energy of the membrane for given values of area and volume are determined by the two shape parameters  $\nu$  and  $\bar{m}$ .<sup>[60]</sup> However, this apparent simplicity hides the morphology complexity which arises from the many energy branches that are “stacked” on top of each other and correspond to multispherical shapes as discussed further below.

## 5.2. Geometry of Two-Sphere Vesicles

The two-sphere vesicles consist of two (punctured) spheres connected by a closed membrane neck. When the two spheres have different sizes, we distinguish the larger sphere with radius  $R_l$  from the smaller sphere with radius  $R_s$ . If both spheres have the same radius  $R_l = R_s$ , we denote this radius by  $R_*$ . We measure all radii in units of the vesicle size  $R_{ve}$  which leads to the dimensionless radii

$$r_l \equiv \frac{R_l}{R_{ve}} \quad \text{and} \quad r_s \equiv \frac{R_s}{R_{ve}} \quad (24)$$

for the large and small spheres and to the radius  $r_* \equiv R_*/R_{ve}$ .

We consider a vesicle with a certain membrane area  $A$  and a certain volume  $V$ . For a two-sphere vesicle, the area  $A$  is equal to  $A_l + A_s$ , that is, to the sum of the large-sphere area  $A_l$  and the small-sphere area  $A_s$ . Likewise, the vesicle volume  $V$  is equal to  $V_l + V_s$  for a two-sphere vesicle with an interior neck

as in Figure 14a and to  $V_l - V_s$  for a two-sphere vesicle with an exterior neck as in Figure 14b. When expressed in terms of the dimensionless radii  $r_l$  and  $r_s$ , the area and volume relations have the simple form<sup>[58, 89]</sup>

$$r_l^2 + r_s^2 = 1 \quad \text{and} \quad \nu = r_l^3 \pm r_s^3 \quad (25)$$

where the plus and minus sign in the second relation corresponds to interior and exterior necks. It is important to note that the two geometric relations in Equation (25) involve only a single parameter, the rescaled volume  $\nu$  introduced in Equation (22), and thus do not depend on any other parameter such as the spontaneous curvature.

### 5.2.1. Two-Sphere Vesicles with Interior Necks

First, let us consider the geometric relations in Equation (25) with the plus sign for interior necks as in Figure 14a, which is formed for positive spontaneous curvature. We then obtain two different sphere radii  $r_l$  and  $r_s$  with

$$r_l > r_s \quad \text{for the volume range} \quad \frac{1}{\sqrt{2}} < \nu \leq 1 \quad (26)$$

as illustrated by the first four panels of Figure 16, where the volume  $\nu$  is reduced from left to right, mimicking the process of osmotic deflation. In addition, the interior neck connects two equally sized spheres with radii

$$r_l = r_s = r_* \equiv \frac{1}{\sqrt{2}} \quad \text{for the special volume} \quad \nu = \frac{1}{\sqrt{2}} \quad (27)$$

as shown in the rightmost panel of Figure 16. The latter shape represents a limit shape, denoted by  $L_{2*}$ , consisting of two equally sized spheres; one experimental example for such a limit shape is shown in Figure 15a.

### 5.2.2. Two-Sphere Vesicles with Exterior Necks

Next, consider the geometric relations in Equation (25) with the minus sign for an exterior neck as in Figure 14b, which is

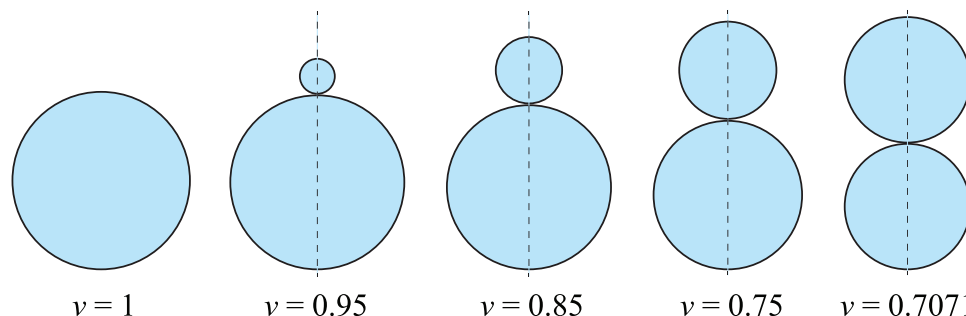


**Figure 16.** Two-sphere vesicles consisting of two (punctured) spheres connected by an interior membrane neck as in Figure 14a. All vesicles have the same surface area but differ in the volume of their interior aqueous solution (blue), which decreases from left to right as indicated by the values of the dimensionless volume  $\nu$  defined in Equation (22), mimicking the process of osmotic deflation. For each vesicle, both spheres have positive mean curvature and can form for positive spontaneous curvature.<sup>[58]</sup> The leftmost shape represents the limiting case, in which the radius of the small sphere vanishes. The rightmost shape represents another limit shape, denoted by  $L_{2*}$ , as provided by two equally sized spheres with the smallest possible volume  $\nu = 1/\sqrt{2} = 0.7071$ .

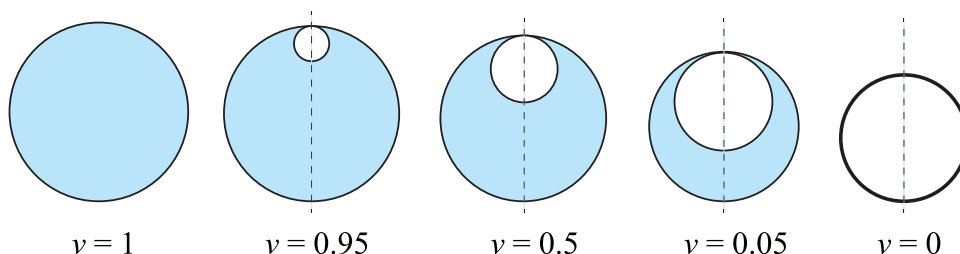


**Figure 17.** Two-sphere vesicles consisting of two nested spheres connected by an exterior membrane neck as in Figure 14b. Such vesicles are formed for negative spontaneous curvature,  $\bar{m} < 0$ . All vesicles have the same surface area but differ in the volume of the interior aqueous solution (blue), as indicated by the values of the dimensionless volume  $\nu$  defined in Equation (22). The leftmost shape represents the limiting case in which the radius of the small sphere vanishes. The rightmost shape represents a limit shape with  $\nu = 0$ , corresponding to two nested spheres of equal size.

formed for negative spontaneous curvature. In this case, the relations describe two nested spheres with

$$r_l > r_s \quad \text{for the volume range } 0 < \nu \leq 1 \quad (28)$$

In addition, vesicles with two nested spheres of equal size are now obtained for volume

$$\nu = 0 \quad \text{with radii } r_l = r_s = \frac{1}{\sqrt{2}} \quad (29)$$

Some examples for such two-sphere vesicles are shown in **Figure 17** where the volume  $\nu$  is reduced from left to right, mimicking the process of osmotic deflation.

### 5.3. Stability of Two-Sphere Vesicles

The stability of the two-sphere vesicles in Figures 16 and 17 depends on three conditions.<sup>[28,29]</sup> First, the closed membrane necks must be stable against neck opening. Second, the individual spheres should be stable against prolate-like deformations. Third, the constriction force acting on the membrane necks should be sufficiently small to avoid neck cleavage and vesicle division. In this subsection, we will focus on the stability of closed necks against neck opening as described by Equations (15) and (16).

When we use the vesicle size  $R_{ve}$  as the basic length scale, the neck stability relations involve the rescaled spontaneous curvature  $\bar{m} = mR_{ve}$  and the rescaled neck curvature  $\bar{M}_{ne} = M_{ne}R_{ve}$ . The rescaled neck curvature

$$\bar{M}_{ne} = \frac{1}{2} \left( \frac{1}{r_l} \pm \frac{1}{r_s} \right) \quad (30)$$

is a purely geometric quantity, which depends only on the rescaled volume  $\nu$ , compare the geometric relationships in Equation (25), and increases monotonically with increasing  $\nu$ . Close to the limiting value  $\nu = 1$ , the small-sphere radius  $r_s$  vanishes and the neck curvature  $\bar{M}_{ne}$  as given by Equation (30) becomes large and positive for interior necks but large and negative for exterior necks, corresponding to the plus and minus sign in this equation.

#### 5.3.1. Two-Sphere Vesicles with Interior Necks

First, consider a closed interior neck as shown in Figure 14a. The stability of such a neck is described by the stability condition in Equation (15). When expressed in terms of rescaled and dimensionless variables, including the rescaled neck curvature  $\bar{M}_{ne} = M_{ne}R_{ve}$ , this stability condition becomes

$$\bar{m} \geq \bar{M}_{ne} = \frac{1}{2} \left( \frac{1}{r_l} + \frac{1}{r_s} \right) \quad (\text{stability of interior neck}) \quad (31)$$

which contains the neck closure condition

$$\bar{m} = \bar{M}_{ne} = \frac{1}{2} \left( \frac{1}{r_l} + \frac{1}{r_s} \right) \quad \text{for } \bar{m} > 0 \quad (32)$$

When we combine this neck closure condition with the geometric relations in Equation (25), using the plus sign for interior necks, we obtain the line of limit shapes  $L_{1+1}$  as plotted in the morphology diagram of **Figure 18a**. In this diagram, the stability regime for the two-sphere vesicles with an interior neck corresponds to the blue shaded region, which is bounded by the line of limit shapes  $L_{1+1}$  from above and by the horizontal line of limit shapes  $L_{2*}$  from below. The latter line describes two-sphere vesicles with two equally sized spheres, see rightmost panel in Figure 16, and corresponds to

$$\nu = \nu_* = \frac{1}{\sqrt{2}} \quad \text{and} \quad \bar{m} \geq \bar{m}_* \equiv \sqrt{2} \quad (33)$$

#### 5.3.2. Two-Sphere Vesicles with Exterior Necks

Second, consider a closed exterior neck as shown in Figure 14b. The stability of such a neck is described by the stability condition in Equation (16). When expressed in terms of rescaled and dimensionless variables, this stability condition becomes

$$\bar{m} \leq \bar{M}_{ne} = \frac{1}{2} \left( \frac{1}{r_l} - \frac{1}{r_s} \right) \quad (\text{stability of exterior neck}) \quad (34)$$

which contains the neck closure condition

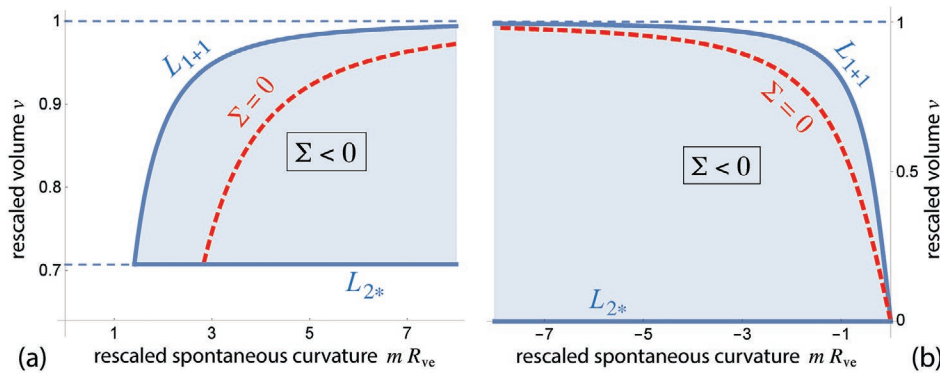


**Figure 18.** Stability regimes (light blue) of two-sphere vesicles as a function of rescaled spontaneous curvature  $\bar{m}$  and rescaled volume  $\nu$  for a) positive and b) negative spontaneous curvatures. Note the different ranges of  $\nu$ -values in the two panels. The two-sphere vesicles consist of two (punctured) spheres connected by a closed membrane neck. Both stability regimes are bounded by two lines, the line of limit shapes  $L_{1+1}$  with  $\bar{m} = \bar{M}_s$  and the line of limit shapes  $L_{2*}$ , consisting of two equally sized spheres. The stability regimes are divided up into two subregimes with positive and negative mechanical tension,  $\Sigma > 0$  and  $\Sigma < 0$ . The mechanical tension vanishes along the red dashed line. In contrast, the total membrane tension  $\Sigma_{\text{tot}} = \Sigma + 2\kappa m^2$  is positive for all two-sphere vesicles.

$$\bar{m} = \bar{M}_{\text{ne}} = \frac{1}{2} \left( \frac{1}{r_l} - \frac{1}{r_s} \right) \quad \text{for } \bar{m} < 0 \quad (35)$$

When we combine this neck closure condition with the geometric relations in Equation (25), using the minus sign for exterior necks, we obtain the line of limit shapes  $L_{1+1}$  as plotted in the morphology diagram of Figure 18b. In this diagram, the stability regime for the two-sphere vesicles with an exterior neck corresponds to the blue shaded region, which is bounded by the line of limit shapes  $L_{1+1}$  from above and by the horizontal line of limit shapes  $L_{2*}$  from below. The latter line describes two nested spheres of equal size, see rightmost panel in Figure 17, and is given by

$$\nu = \nu_* = 0 \quad \text{and} \quad \bar{m} \leq \bar{m}_* \equiv 0 \quad (36)$$

### 5.3.3. Membrane Tensions of Two-Sphere Vesicles

The mechanical membrane tension  $\Sigma$  of the two-sphere vesicle is given by<sup>[28, 89]</sup>

$$\Sigma = 2\kappa m(2M_{\text{ne}} - m) = 2\kappa m(M_l + M_s - m) \quad (37)$$

which depends on the neck curvature  $M_{\text{ne}}$ . The latter curvature can be expressed in terms of the curvature radii  $R_l$  and  $R_s$ , see Equations (13) and (14) for interior and exterior necks. The tension–curvature relationship in Equation (37) shows explicitly that the mechanical membrane tension depends, via the neck curvature  $M_{\text{ne}}$ , on the two spherical radii  $R_l$  and  $R_s$  and, thus, on the size and shape of the two-sphere vesicle.

When we add the spontaneous tension  $2\kappa m^2$  to the mechanical tension  $\Sigma$ , we obtain the total membrane tension

$$\Sigma_{\text{tot}} = \Sigma + 2\kappa m^2 = 4\kappa m M_{\text{ne}} = 2\kappa m \left( \frac{1}{R_l} \pm \frac{1}{R_s} \right) \quad (38)$$

where the plus and minus sign applies to interior and exterior necks as before. The latter expression can be directly derived from the two shape equations

$$\Delta P = 2\Sigma_{\text{tot}} M_{\text{sp}} - 4\kappa m M_{\text{sp}}^2 \quad \text{for } M_{\text{sp}} = M_l \text{ and } M_{\text{sp}} = M_s, \quad (39)$$

by eliminating the pressure difference  $\Delta P$  from these equations.<sup>[73]</sup> Even though this derivation does not “know” about the closed membrane neck, the dependence of the total membrane tension on the vesicle geometry is encoded in the neck curvature  $M_{\text{ne}}$ .

For a two-sphere vesicle with an interior neck, both the spontaneous curvature  $m$  and the neck curvature  $M_{\text{ne}}$  are positive which implies that the total membrane tension  $\Sigma_{\text{tot}}$  in Equation (38) is positive as well. For a two-sphere vesicle with an exterior neck, both the spontaneous curvature  $m$  and the neck curvature  $M_{\text{ne}}$  are negative which leads again to a positive total tension  $\Sigma_{\text{tot}}$ . Therefore, the total membrane tension is positive for all two-sphere vesicles. In contrast, the mechanical tension  $\Sigma$  turns out to be negative for a large range of parameters.

The limit shapes  $L_{1+1}$  in the morphology diagram of Figure 18 are characterized by the neck closure condition  $M_{\text{ne}} = m$ . When this equality is inserted into Equation (37), the mechanical tension becomes

$$\Sigma = 2\kappa m^2 = \sigma \quad \text{for all limit shapes } L_{1+1} \quad (40)$$

that is, the mechanical tension  $\Sigma$  is always positive and equal to the spontaneous tension  $\sigma$  for the limit shapes  $L_{1+1}$ . This equality holds for both positive and negative spontaneous curvature, see the corresponding lines  $L_{1+1}$  in Figure 18a,b. It also follows from Equation (37) that

$$\Sigma = 0 \quad \text{for} \quad 2M_{\text{ne}} = \frac{1}{R_l} \pm \frac{1}{R_s} = m \quad (41)$$

corresponding to the red dashed lines in Figure 18a,b. Furthermore, along the line of limit shapes  $L_{2*}$  in Figure 18a,b, the mechanical tension is given by

$$\Sigma = 2\kappa m \left( \frac{2\sqrt{2}}{R_{ve}} - m \right) \approx -2\kappa m^2 \quad \text{for } L_{2^*} \text{ and } m \geq \frac{\sqrt{2}}{R_{ve}} \quad (42)$$

where the asymptotic equality, as indicated by the  $\approx$  symbol, holds for large positive  $m$ , and by

$$\Sigma = -2\kappa m^2 \quad \text{for } L_{2^*} \text{ and } m < 0 \quad (43)$$

As mentioned, the shape of a two-sphere vesicle depends only on  $\nu$  and, thus, does not change as we vary the spontaneous curvature  $\bar{m}$  for constant  $\nu$ , which corresponds to a horizontal trajectory within the stability regimes in Figure 18a,b. Likewise, the neck curvature  $2M_{ne} = M_l + M_s$  remains constant along such a horizontal trajectory. It then follows from Equation (37) that the mechanical tension  $\Sigma \approx -2\kappa m^2$ , that is, this tension becomes more and more negative as we go to large positive or large negative spontaneous curvatures. At the same time, the constriction force  $f$  increases as  $8\kappa|m|$  as follows from Equations (18) and (19). Therefore, the enhancement of the constriction force is accompanied by an increased compression of the vesicle membrane, both for positive and for negative spontaneous curvature.

## 6. Multispherical Shapes of Vesicles

The two-sphere vesicles discussed in the previous section represent the simplest examples for stable multispherical or “multi-balloon” shapes. Indeed, the theory of curvature elasticity predicts stable  $(N_l + N_s)$ -multispheres consisting of  $N_l$  large and  $N_s$  small spheres connected by closed membrane necks for arbitrary values of  $N_l$  and  $N_s$ . As for the two-sphere vesicles, we can again distinguish interior and exterior necks, see Figure 14, which are formed for positive and negative spontaneous curvature, respectively. In the following, we will focus on positive spontaneous curvature and interior membrane necks because this case has also been studied experimentally in a systematic manner.

### 6.1. Multispheres from Curvature Elasticity

All  $(N_l + N_s)$ -multispheres with up to three spheres are depicted in Figure 19 for positive spontaneous curvature. All of these

multispheres are connected by interior necks as introduced in Figure 14a. As far as two-sphere vesicles are concerned, we now distinguish  $(1 + 1)$ -multispheres, for which the two individual spheres have two different radii, from  $(2^*)$ -multispheres, for which both spheres have the same radius, see the two boxes labeled by  $(1 + 1)$  and  $(2^*)$  in Figure 19. These two-sphere shapes involve only a single membrane neck: the  $ls$  neck between the large and the small sphere for the  $(1 + 1)$ -multisphere and the  $**$  neck for the  $(2^*)$ -multisphere. However, as soon as we consider multispherical shapes with more than two spheres, these shapes can involve different types of necks.

One example is provided by the left multisphere pattern in the  $(1 + 2)$  box of Figure 19, which involves both an  $ls$  and an  $ss$  neck between two small spheres. Another example is the right multisphere in the  $(2 + 1)$  box of Figure 19, which involves both an  $ls$  neck and an  $ll$  neck between two large spheres. Inspection of the  $(1 + 2)$  box of Figure 19 also reveals that we must distinguish two different patterns of  $(1 + 2)$ -multispheres: one pattern involves one  $ls$  and one  $ss$  neck whereas the other pattern involves two  $ls$  necks. Likewise, the  $(2 + 1)$  box of Figure 19 contains one pattern with two  $ls$  necks and one pattern with one  $ls$  and one  $ll$  neck. We use the term “multisphere pattern” to distinguish different connectivities for the same number of  $N_l$  large and  $N_s$  small spheres. These different patterns have the same vesicle volume  $V$  but will, in general, differ in the types of necks that connect the spheres.

The number of different patterns for  $(N_l + N_s)$ -multispheres increases with the number of spheres. This increasing complexity is illustrated in Figure 20 which displays the possible multispherical patterns with four spheres that a vesicle of fixed area can form. Inspection of Figures 19 and 20 shows that we have two patterns for  $(1 + 2)$ - and  $(2 + 1)$ -multispheres, four patterns for  $(1 + 3)$ -multispheres, six patterns for  $(2 + 2)$ -multispheres, and four patterns for  $(3 + 1)$ -multispheres. Likewise, we have one pattern for  $(2^*)$ - and  $(3^*)$ -multispheres and two patterns for  $(4^*)$ -multispheres. All multispheres considered here are tree-like in the graph-theoretic sense and do not contain a subset of spheres that form a closed cycle. Such cycles could be generated if we considered the possibility of membrane fusion between different spheres. Note also that the total number of multisphere patterns increases from 5 for three spheres (Figure 19) to 16 for four spheres (Figure 20).

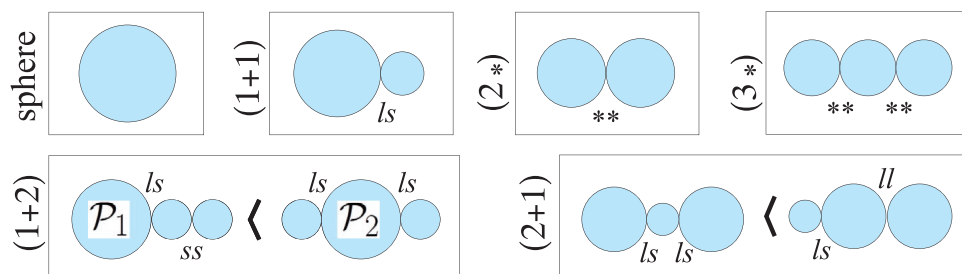


**Figure 19.** Different  $(N_l + N_s)$ -multispherical or “multi-balloon” vesicles with  $N_l + N_s \leq 3$  as well as  $(N^*)$ -multispheres with  $N^* = 2$  and  $N^* = 3$  equally sized spheres, as predicted theoretically. All multispheres displayed here have the same membrane area and can be obtained from the spherical vesicle in the upper left box by reducing the vesicle volume (light blue). Each contact point between two spheres contains a closed interior neck as in Figure 14a, which implies that each multisphere is formed by a single membrane. The  $(N_l + N_s)$ -multispheres can involve three types of membrane necks, denoted by  $ls$ ,  $ss$ , and  $ll$ . The  $(N^*)$ -multispheres involve only a single type of neck, denoted by  $**$ . Both the  $(1 + 2)$ -multispheres and the  $(2 + 1)$ -multispheres can form two distinct multisphere patterns. In both cases, the two distinct patterns have the same volume. The  $<$  symbol indicates the relative stability of the two  $(1 + 2)$  and the two  $(2 + 1)$  patterns, labeled by  $\mathcal{P}_1$  and  $\mathcal{P}_2$  in the  $(1 + 2)$  box, arising from the least stable necks, see main text.

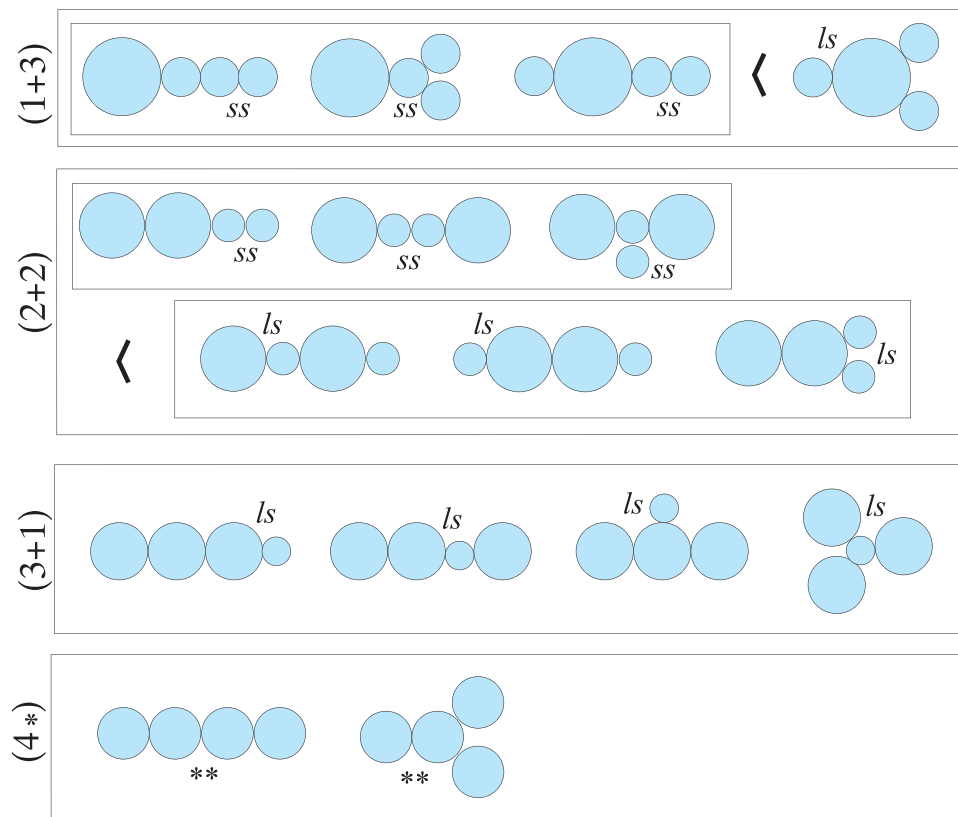


**Figure 20.** Different patterns of multispheres or “multi-balloons” with four spheres. All 16 multisphere patterns can again be obtained from the spherical vesicle in the upper left corner of Figure 19 by reducing the vesicle volume for conserved membrane area. All multispheres with the same values of  $N_l$  and  $N_s$  have the same volume. As in Figure 19, each contact point between two spheres contains an interior membrane neck and each multisphere pattern is formed by a single membrane that encloses the whole vesicle volume (light blue). For visual clarity, only one of the least stable necks, which can be an *ss*, *ls*, or *\*\** neck, is labeled. Note that 7 out of 16 patterns with four spheres contain a three-way junction, provided by one sphere that is connected to three other spheres.

### 6.1.1. Geometry of $(N_l + N_s)$ -Multispheres

The geometry of the multispheres displayed in Figures 19 and 20 is obtained by generalizing the geometric relations for the case of two-sphere vesicles, see Equation (25). As before, we consider a vesicle of volume  $V$  which is bounded by a membrane of surface area  $A$ . We take the vesicle size  $R_{ve} = \sqrt{A/(4\pi)}$  to be the basic length scale and define the dimensionless large-sphere radius  $r_l = R_l/R_{ve}$  and small-sphere radius  $r_s = R_s/R_{ve}$ . The geometry of all possible  $(N_l + N_s)$ -multispheres is then described by<sup>[58,89]</sup>

$$N_l r_l^2 + N_s r_s^2 = 1 \quad \text{and} \quad N_l r_l^3 + N_s r_s^3 = \nu \quad (44)$$

which depend now on three parameters, on the large-sphere and small-sphere numbers  $N_l$  and  $N_s$  as well as on the dimensionless volume  $\nu$  defined in Equation (22). For the special case of  $N_*$  equally sized spheres with  $r_l = r_s = r_*$ , the geometric relations in Equation (44) simplify and become

$$N_* r_*^2 = 1 \quad \text{and} \quad N_* r_*^3 = \nu \quad (45)$$

which leads to the sphere radius  $r_* = 1/\sqrt{N_*}$  and to the volume  $\nu = \nu_* = 1/\sqrt{N_*}$ .

The stability of the multispheres again involves three conditions: the stability of the closed necks against neck opening; the stability of individual spheres against the sphere-prolate instability; and the stability of the necks against membrane fission. We will again focus on the stability of closed necks as described in the next paragraphs.

### 6.1.2. Stability of Different Types of Necks

As illustrated in Figures 19 and 20, a multisphere pattern with more than two spheres may involve different types of necks which differ in their neck curvature and, thus, in their stability. A certain multisphere pattern is stable against neck opening if all closed necks are stable.

To discuss the different necks and their stability, we will first distinguish their neck curvature by introducing the notation

$$M_{ab} \equiv \frac{1}{2}(M_a + M_b) = \frac{1}{2}\left(\frac{1}{R_a} + \frac{1}{R_b}\right) \quad (46)$$

for closed interior necks connecting a sphere of mean curvature  $M_a = 1/R_a$  with a sphere of mean curvature  $M_b = 1/R_b$  where both subscripts  $a$  and  $b$  can be equal to  $l$  or  $s$  or  $*$ . The subscript

\* corresponds to the special case of multisphere patterns that consist of  $N_* = N_l + N_s$  equally sized spheres. Thus, an  $ll$ ,  $ls$ ,  $ss$ , and  $**$  neck has neck curvature  $M_{ll}$ ,  $M_{ls}$ ,  $M_{ss}$ , and  $M_{**}$ , respectively. Because  $R_s < R_l$  and  $M_s > M_l$ , these neck curvatures are ordered according to

$$M_{ll} < M_{ls} < M_{ss} \quad (47)$$

For the special case of a multisphere that consists of  $N_* = N_l + N_s$  equally sized spheres, the large-sphere and small-sphere radii become equal, with  $R_l = R_s = R_*$ , and the neck curvature  $M_{**} = 1/R_* = \sqrt{N_*}/R_{ve}$ .

The stability condition for a closed neck as given by Equation (15) now becomes

$$m \geq M_{ab} > 0 \quad \text{with } M_{ab} = M_{ss} \text{ or } M_{ls} \text{ or } M_{ll} \text{ or } M_{**} \quad (48)$$

For an  $ls$ -neck, we obtain the stability condition  $M_{ls} \leq m$  which has the same form as for the single neck of a  $(1 + 1)$ -sphere. Likewise, the observation of a stable  $ss$ - and  $ll$ -neck implies  $m \geq M_{ss} = R_s^{-1}$  and  $m \geq M_{ll} = R_l^{-1}$ , respectively. When a multispherical shape exhibits several types of membrane necks, this shape is only stable if all of its necks are stable against neck opening. Because the neck curvatures are ordered according to  $M_{ll} < M_{ls} < M_{ss}$ , a sufficiently large spontaneous curvature  $m$  that exceeds the curvature  $M_{ss}$  of the  $ss$  neck ensures that all necks are stable.

### 6.1.3. Stability Regimes of Multisphere Patterns

Each  $(N_l + N_s)$ -multisphere pattern is stable within a certain parameter regime that is governed by the stability of its least stable neck. The least stable neck may be different for different multisphere patterns that can be formed by the same numbers of large and small spheres. Examples for such stability differences are found for the two patterns of  $(1 + 2)$ - and  $(2 + 1)$ -multispheres in Figure 19 as well as for the four patterns of  $(1 + 3)$ -multispheres and for the six patterns of  $(2 + 2)$ -multispheres in Figure 20. Consider, for instance, the two  $(1 + 2)$ -multisphere patterns,  $\mathcal{P}_1$  and  $\mathcal{P}_2$ , in Figure 19. The stability of the  $\mathcal{P}_1$  pattern, which involves one  $ss$  and one  $ls$  neck, is determined by the neck curvature  $M_{ss}$  of the  $ss$  neck and the stability condition  $m \geq M_{ss}$ . The stability of the  $\mathcal{P}_2$  pattern, which involves two  $ls$  necks, is determined by these identical necks and the corresponding stability condition  $m \geq M_{ls}$ . The inequality  $M_{ls} < M_{ss}$  then implies that the pattern  $\mathcal{P}_2$  has an enlarged stability regime compared to the pattern  $\mathcal{P}_1$  as long as we ignore transmutations between these two patterns, see further below. This enhanced stability regime of the  $\mathcal{P}_2$  pattern is indicated by the  $\langle$  symbol in Figure 19.

As for the case of  $(1 + 1)$ -multispheres, see Figure 18, each multisphere pattern is stable against neck opening within a certain stability regime of the morphology diagram. This stability regime is located between two lines of limit shapes, the line of limit shapes  $L_{N_l + N_s}$ , at which the least stable neck closes, and the line of limit shapes  $L_{N_*}$ , corresponding to  $N_* = N_l + N_s$  equally sized spheres. The least stable neck will in general be different for different multisphere patterns with the

same number of large and small spheres, see Figures 19 and 20, which implies that the line of limit shapes  $L_{N_l + N_s}$  for these different patterns will be somewhat different as well. In contrast, the line of limit shapes  $L_{N_*}$  is always determined by the  $**$  necks with neck curvature  $M_{**} = 1/R_* = \sqrt{N_l + N_s}/R_{ve}$ . For positive spontaneous curvatures, the limit shapes  $L_{N_*}$  are found at

$$\nu = \nu_* \equiv \frac{1}{\sqrt{N_l + N_s}} \quad \text{and} \quad \bar{m} \geq \bar{m}_* \equiv \sqrt{N_l + N_s} \quad (49)$$

Thus, all  $(N_l + N_s)$ -multisphere patterns are located above this horizontal line in the morphology diagram.

Each stability regime of the different multispheres and multisphere patterns leads to a different branch of the bending energy.<sup>[28,58,114]</sup> Furthermore, the different stability regimes strongly overlap with each other, which implies that we typically find a large number of different branches of the bending energy for a given point in the morphology diagram. These different branches are stacked on top of each other and constitute a complex and rugged landscape of the bending energy.

### 6.1.4. Membrane Tensions of Multispheres

For  $(N_l + N_s)$ -multispheres, the mechanical membrane tension is given by

$$\Sigma = 2\kappa m(2M_{ls} - m) = 2\kappa m(M_l + M_s - m) \quad (50)$$

which has the same form as Equation (37) for  $(1 + 1)$ -multispheres with the neck curvature  $M_{ne}$  being replaced by  $M_{ls}$ , the neck curvature of an  $ls$  neck. In the limit, in which all spheres attain the same radius  $R_l = R_s = R_*$ , all necks become  $**$  necks and the neck curvature  $M_{ls}$  becomes equal to  $M_{**} = 1/R_*$ . Note that the tension–curvature relationship in Equation (50) does not depend on the sphere numbers  $N_l$  and  $N_s$  explicitly but depends on these numbers only implicitly via the radii  $R_l$  and  $R_s$ , as follows from the geometric relations in Equation (44).

Two-sphere vesicles or  $(1 + 1)$ -multispheres are special in the sense that they involve only a single  $ls$  neck with neck curvature  $M_{ne} = M_{ls}$ , which determines both the stability of the multispherical shape and the mechanical tension. In contrast, the stability of  $(N_l + N_s)$ -multispheres with more than one neck depends on the neck curvature of the least stable neck, which is often provided by an  $ss$  neck and the associated neck curvature  $M_{ss}$ , whereas the mechanical tension is always determined by the neck curvature  $M_{ls}$  of the  $ls$  neck as in Equation (50).

The mechanical tension vanishes for  $m = 2M_{ls}$  which partitions the stability regime of each  $(N_l + N_s)$ -multispherical pattern into two subregimes, a small one with positive mechanical tension and a large one with negative mechanical tension, in close analogy to the partitioning of the stability regime for  $(1 + 1)$ -multispheres as displayed in Figure 18. For the special case of  $N_*$  equally sized spheres with neck curvature  $M_{**} = 1/R_* = \sqrt{N_*}/R_{ve}$ , the mechanical tension becomes  $\Sigma = 2\kappa m(\sqrt{N_*}/R_{ve} - m)$  for spontaneous curvature  $m \geq m_* = \sqrt{N_*}$  which implies  $\Sigma = 2\kappa N_*/R_{ve}^2$  at the corner point with  $m_* = \sqrt{N_*}/R_{ve}$ .<sup>[28]</sup> For all  $(N_l + N_s)$ -multispheres, the mechanical

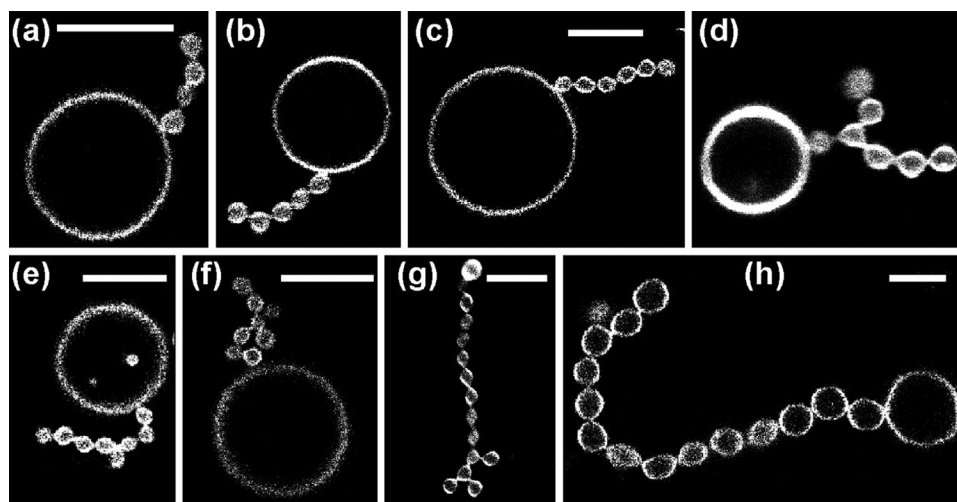


**Figure 21.** Patterns of  $(1 + N_s)$ -multispheres or “multi-balloons” formed by giant vesicles, which were exposed to asymmetric sucrose–glucose solutions.<sup>[28]</sup> The multisphere patterns displayed here consist of one large sphere and a linear or branched tubule with  $N_s \geq 4$  small spheres: Linear tubule with a)  $N_s = 4$ , b)  $N_s = 5$ , and c)  $N_s = 6$ . Branched tubule with d)  $N_s = 7$ , e, f)  $N_s = 8$ , g)  $N_s = 14$ , and h)  $N_s = 15$ . Each branched tubule contains three-way junctions, consisting of one small sphere that is connected to three other small spheres. All scale bars are  $10 \mu\text{m}$ . Reproduced under terms of the CC-BY license.<sup>[28]</sup> Copyright 2020, The Authors, published by Royal Society of Chemistry.

tension becomes large and negative both for large positive and for large negative spontaneous curvatures.

## 6.2. Experimental Observations of Stable Multispheres

A striking variety of multisphere patterns has been recently observed in experimental studies of giant vesicles that were exposed to asymmetric sugar solutions.<sup>[28]</sup> Some relatively simple examples with  $N_l + N_s \leq 4$  are shown in the introductory Figure 6. Indeed, this figure displays a  $(1 + 1)$ -multisphere in panel (a), two  $(1 + 2)$ -multisphere patterns in panels (b) and (c), a  $(2 + 1)$ -multisphere in panel (d), a  $(1 + 3)$ -multisphere in panel (e), two  $(2 + 2)$ -multisphere patterns in panels (f) and (g), as well as a  $(3 + 1)$ -multisphere in panel (h). More complex multisphere patterns that consist of more than four spheres have also been observed, see the optical images in Figures 21 and 22.

The microscopy images in Figures 21 and 22 confirm several general features of multispheres as predicted by the theory of curvature elasticity. First, each multisphere is formed by a single membrane which encloses the whole vesicle volume. Second, each multisphere involves only two different sphere radii, the large-sphere radius  $R_l$  and the small-sphere radius  $R_s$ , which is a direct consequence of the shape equation as obtained from the first variation of the bending energy. Third, the observed multisphere patterns are all located within the stability regimes predicted by the theory.<sup>[28]</sup>

### 6.2.1. Transmutations between Different Multisphere Patterns

The experimental observations also revealed that the small spheres are rather mobile and can be rearranged by diffusion of the  $ss$  necks between two small spheres.<sup>[28]</sup> In this way, a given sphere pattern can be transmuted into another sphere pattern, built up from the same numbers of large and small

spheres. One frequent transmutation was observed for tubules of small spheres, see examples in Figures 21 and 22, which underwent transitions between linear and branched tubules. During these transitions, one small sphere diffused along another small sphere, corresponding to the diffusion of an  $ss$  neck, until this neck was transferred onto a third small sphere, thereby generating a three-way junction between four small spheres.

The diffusion of a small sphere along a large sphere, corresponding to the diffusion of an  $ls$  neck, should also occur quite frequently because this diffusion process is not expected to encounter any energy barrier.<sup>[115]</sup> What is less obvious is that a diffusing  $ls$  neck can be transferred onto a second small sphere which is also connected to the large sphere. Such a transfer would change the  $ls$  neck into an  $ss$  neck which may involve a substantial energy barrier.

As an example, let us consider the two  $(1 + 2)$ -multisphere patterns,  $\mathcal{P}_1$  and  $\mathcal{P}_2$ , in Figure 19. The pattern  $\mathcal{P}_1$  on the left involves one  $ls$  and one  $ss$  neck whereas the pattern  $\mathcal{P}_2$  on the right involves two  $ls$  necks. Both patterns have been observed for giant vesicles, see the optical images of the two patterns in Figure 6b,c. To transmute the  $\mathcal{P}_2$  pattern into the  $\mathcal{P}_1$  pattern, one  $ls$  neck must first diffuse over the membrane of the large sphere until the two small spheres are close together. In a second step, the  $ls$  neck can then be transferred onto the second small sphere, thereby transforming the  $ls$  neck into an  $ss$  neck.

So far, such a transmutation process from pattern  $\mathcal{P}_2$  to pattern  $\mathcal{P}_1$  has not been observed directly but could become accessible if one monitors the long-time behavior of pattern  $\mathcal{P}_2$  as displayed in Figure 6c. Indeed, if pattern  $\mathcal{P}_2$  were transmuted into pattern  $\mathcal{P}_1$ , the new  $ss$  neck may be unstable and open up, because the stability regime of the  $\mathcal{P}_1$  pattern is smaller than the stability regime of the  $\mathcal{P}_2$  pattern as indicated by the  $\langle$  symbol in the  $(1+2)$  box of Figure 19. Therefore, the transmutation of the  $\mathcal{P}_2$  into the  $\mathcal{P}_1$  pattern can lead to a stable  $\mathcal{P}_1$  pattern or to another shape without an  $ss$  neck.

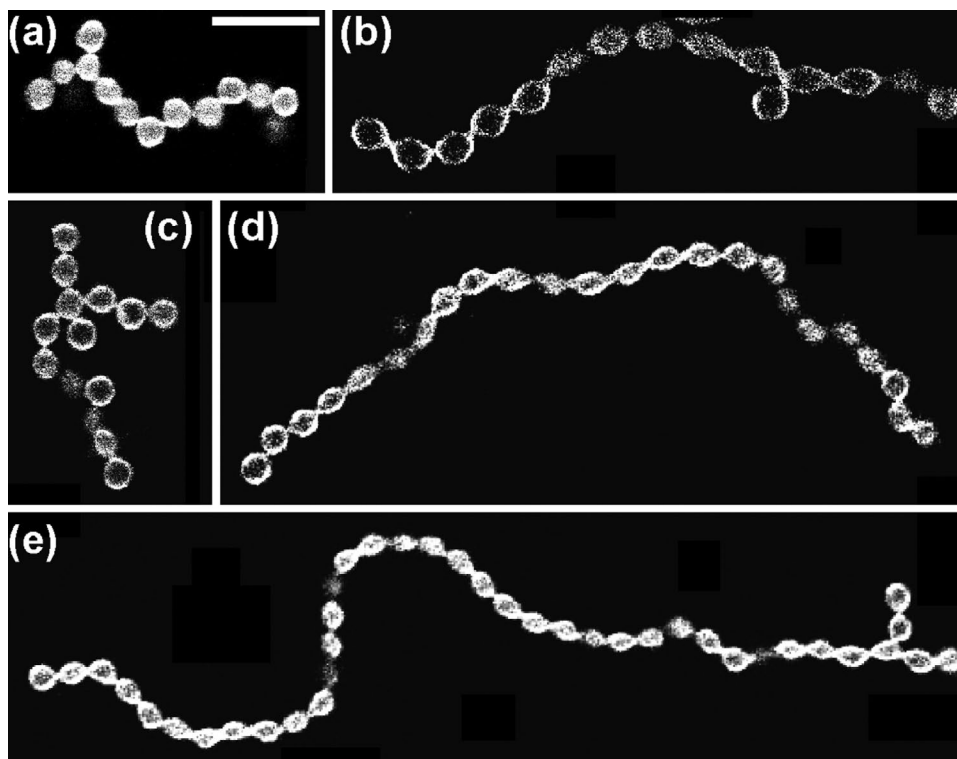


**Figure 22.** Patterns of ( $N^*$ )-multispheres formed by giant vesicles that were exposed to asymmetric sucrose–glucose solutions.<sup>[28]</sup> Each pattern shown here forms a branched or linear tubule with  $N_*$  equally sized spheres: a) Branched chain with  $N_* = 14$ . Twelve of these spheres are clearly visible. In addition, one sphere, located at the right chain end, is out of focus and another one, connected to the second sphere from the left is hardly visible. b) Branched chain with  $N_* = 15$ ; c) Another branched chain with  $N_* = 15$ . Fourteen of these spheres are visible, another one is hidden behind the bottom sphere; d) Linear chain with  $N_* = 24$ ; and e) Branched chain with  $N_* = 39$ . The precise number of small spheres has been obtained from the analysis of the corresponding time-lapse movies. Such movies also revealed three-way junctions in (a), (b), and (e) as well as the presence of a four-way junction in (c). The scale bar in (a) is 10  $\mu\text{m}$  and applies to all panels. Reproduced under terms of the CC-BY license.<sup>[28]</sup> Copyright 2020, The Authors, published by Royal Society of Chemistry.

### 6.3. Junctions of Membrane Tubules

The multispherical tubules in Figure 21d and in several panels of Figure 22 contain tubular junctions, corresponding to individual spheres that are connected to more than two neighboring spheres. The analysis of the corresponding time-lapse movies<sup>[28]</sup> shows that most of these junctions are three-way junctions, with some exceptions, such as the junction in Figure 22c which represents a four-way junction.

Stable three-way junctions have also been observed for the nanotubular network of the endoplasmic reticulum whereas stable four-way junctions have been difficult to detect.<sup>[2,4,5,116,117]</sup> As far as membrane elasticity is concerned, there are two main differences between the membrane tubules formed by giant vesicles as discussed here and the membrane nanotubes of the reticular networks. First, the tubules displayed in Figures 21 and 22 have a diameter of about 2  $\mu\text{m}$  whereas the nanotubes of the reticular networks have a diameter of about 50–100 nm, as has been deduced from electron microscopy. Therefore, the membranes of the reticular networks have a much larger spontaneous curvature. Second, the tubules formed by the giant vesicles undergo strong bending fluctuations in response to thermal noise. In contrast, the tubular segments between two junctions of the reticular networks appear to be rather straight, indicating the presence of a substantial membrane tension.

To get some insight into this difference in the tubular morphology, let us consider a three-way junction as in Figure 21d but imagine that it consists of a larger number of small spheres as in Figure 22e. The junction contains a specific small sphere, which forms the junctional center. This center is linked via three *ss* necks to three linear tubules or junctional arms. Two of these arms have a free end while one arm is connected to the large sphere via an *ls* neck. The free ends undergo strong thermal fluctuations whereas the *ls* end is constrained to move on the surface of the large sphere. We will now perform some Gedanken experiments with this junction.

First, we aspirate the large sphere by a micropipette and grasp one of the free ends by a laser trap to exert a pulling force on it. We will then encounter several distinct force regimes. First, we will straighten two arms of the junction until the pulled free end becomes collinear with the junctional center and the *ls* end. At this point, the third junctional arm will still undergo strong thermal fluctuations. When we further increase the pulling force, the small spheres of this third arm will be drawn into the straightened tube segment until all small spheres are part of this segment. So far, the number of small spheres has been conserved and we have arrived at a straight tubule consisting of all small spheres that formed the original junction. However, when we continue to increase the pulling force even further, we may start to open up the closed necks between

the small spheres. As a result, the multispherical tubule will be transformed into an unduloidal or cylindrical tubule.<sup>[83]</sup> Because the necks experience a curvature-induced constriction force as given by Equation (18), the opening of the closed necks is expected to require a pulling force that exceeds a certain threshold value.

Alternatively, we may use two laser traps to exert pulling forces on both free ends of the three-way junction considered here. These two pulling forces will act to straighten all three arms simultaneously. At the same time, the applied forces will be transmitted to the junctional center and the three arms will exert three forces onto this center. These three forces will initially be unbalanced and add up to a nonzero force acting on the center. The junction will then start to move until the three forces acting on the center add up to zero force. This force balance implies that the junctional arms form a contact angle of  $360/3 = 120$  degrees at the junctional center. The latter contact angle is the angle typically observed for reticular networks of nanotubes.

Now, let us extend these considerations to a four-way junction, again consisting of a large number of spheres, as displayed in **Figure 23a**. The junction is taken to experience a significant tension which leads to four straight arms of the junction. Force balance now implies that the contact angle between two neighboring arms is equal to  $360/4 = 90$  degrees. The membrane tension contributes an elastic energy that is proportional to the total length of the junctional arms. Because the membrane tubules of the four-way junction are fluid, this junction can be divided up into two three-way junctions as shown in **Figure 23b**, with contact angles of 120 degrees at both three-way junctions. It turns out that the total length of the tubules in **Figure 23b** is smaller than the total length of the four-way junction in **Figure 23a** which implies that the mechanical membrane tension and the membrane's elastic energy are reduced when we transform the four-way junction into two three-way junctions. As a consequence, we conclude that membrane tubules under tension prefer to form three-way rather than four-way junctions in agreement with the experimental observations on the reticular networks of nanotubes.

## 7. Remodeling of Membrane Topology

The remodeling processes of membranes as described in the previous sections involved striking shape transformations but did not change the topology of the membrane compartments. Thus, even the multispherical shapes consisting of many spheres connected by closed necks have the same topology as a spherical vesicle because they can be smoothly transformed into a single sphere by osmotic inflation. In the following, we will now consider remodeling processes that involve membrane fission and fusion, both of which change the topology of the membranes.

### 7.1. Different Topologies of Membrane Compartments

Membrane compartments and vesicles are closed surfaces, the topology of which depends only on one integer number, the so-called Euler characteristic  $\chi$ . This characteristic is defined for

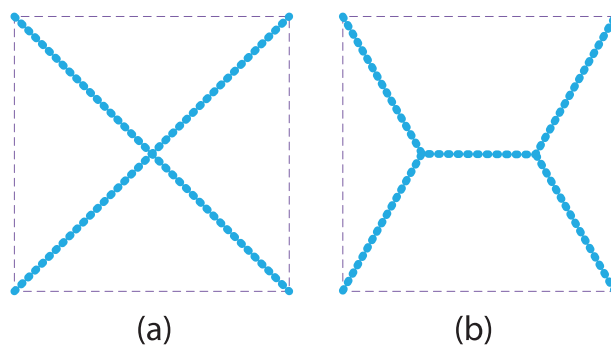


**Figure 23.** Junctions of membrane tubules. Because the tubules are fluid, force balance at the junction implies that all contact angles between neighboring tubules have the same value: a) Four-way junction with all contact angles equal to 90 degrees; and b) Two three-way junctions with all contact angles equal to 120 degrees. The total length of the tubules in (a) is somewhat larger than the total length of the tubules in (b), which implies a reduction in the elastic membrane energy when we transform the four-way junction into two three-way junctions. The resulting tube pattern with two three-way junctions represents a simple example of a Steiner minimal tree<sup>[118–121]</sup> as studied in mathematical graph theory.

any partitioning of the membrane surface into a discrete set of surface segments.<sup>[57]</sup> One widely applied discretization method is triangulation but one may also use a mesh of smooth curves that are embedded in the surface. Any discretization involves the surface segments themselves, which are usually called “faces,” the edges between neighboring faces, and the vertices at which several edges come together. The Euler characteristic  $\chi$  is then defined by

$$\chi = F - E + V \quad (51)$$

where  $F$ ,  $E$ , and  $V$  is the number of faces, edges, and vertices, respectively. These three numbers depend on the chosen partitioning of the surface as one can easily see by using a tetrahedron, a cube or an icosahedron as simple discretization of a sphere and counting  $F$ ,  $E$ , and  $V$  for these different polyhedra. In contrast, the Euler characteristic  $\chi$  itself is independent of this partitioning and defines the topology of the surface. Thus, we obtain  $\chi = 2$  for a tetrahedron, a cube, or an icosahedron as well as for any other discretization of a spherical surface.

Three simple examples for closed membrane surfaces which differ in their Euler characteristic are displayed in **Figure 24**. The torus or doughnut-like shape on the left has the Euler characteristic  $\chi = 0$ , the sphere has  $\chi = 2$ , and the combined surface of two spheres has  $\chi = 4$ . Likewise, the topology of  $N_{ve}$  separate spherical compartments is characterized by  $\chi = 2N_{ve}$  and the topology of a sphere with  $N_{ha}$  handles by  $\chi = 2 - 2N_{ha}$ .

#### 7.1.1. Topological Remodeling by Fusion and Fission

By definition, a topological transformation of a membrane compartment or vesicle changes its topology and, thus, its Euler characteristic. In the living cell, the organelle membranes continuously undergo such topological transformations by membrane fission (or scission) and by membrane fusion, as illustrated in **Figure 1**. Likewise, the simple shapes in **Figure 24**

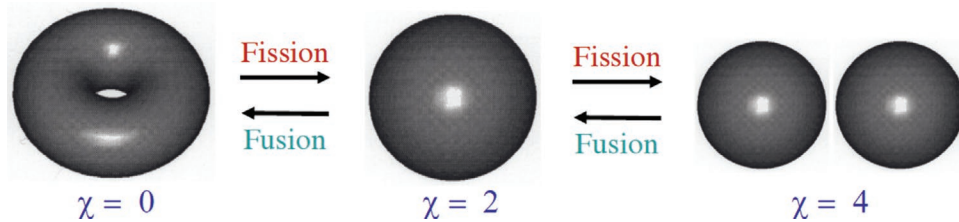


**Figure 24.** Closed membrane compartments with different topologies as distinguished by their Euler characteristic  $\chi$ : A torus (or doughnut) with  $\chi = 0$ , a sphere with  $\chi = 2$ , and two spheres with  $\chi = 4$ . Membrane fission (or scission) increases the Euler characteristic  $\chi$  whereas membrane fusion decreases  $\chi$ . Fission can be used to create a large number  $N_{ve}$  of vesicles with a large positive Euler characteristic,  $\chi = 2N_{ve}$ . Fusion of toroidal vesicles can be used to create membrane surfaces with a large number  $N_{ha}$  of handles and a large negative Euler characteristic,  $\chi = 2 - 2N_{ha}$ .

can also be connected by fission and fusion processes. The torus in Figure 24 can be smoothly deformed into a stomatocyte with two exterior necks and fission of one neck leads to a shape with spherical topology. The fission of a sphere leads to two spheres. On the other hand, fusion of two spheres leads to a single sphere which we can then transform into a torus by another fusion step. One possible shape transformation to facilitate the latter fusion process is to first deflate the sphere, thereby obtaining a discocyte with both of its poles in close proximity, and subsequently fuse the membrane segments of these two poles.

A single fission process always leads to an increase of the Euler characteristic by  $\Delta\chi = +2$  whereas a single fusion process always leads to a decrease of  $\chi$  by  $\Delta\chi = -2$ . These values of  $\Delta\chi$  for individual fission and fusion events are completely general and apply to all vesicle shapes as long as each vesicle membrane forms a closed surface without bilayer pores or bilayer edges, both before and after the events. Therefore, computing the Euler characteristic of two membrane compartments provides a simple and general method to distinguish fission and fusion processes which is not always obvious. One membrane process in the cell for which fission has often been confused with fusion is the closure of an autophagosome.<sup>[122]</sup>

It is interesting to note that the preparation of synthetic vesicles also involves topological transformations and associated changes of the Euler characteristic. Consider, for example, the formation of  $N_{ve}$  vesicles from a planar, solid-supported membrane and assume that the planar bilayer has  $N_{po}$  additional bilayer pores after the vesicle formation. The changed topology of the membrane then implies the change  $\Delta\chi = 2N_{ve} - N_{po}$  of the Euler characteristic, which does not depend on the shapes of vesicles and pores.

### 7.1.2. Curvature Elasticity of Topological Transformations

The Euler characteristic is intimately related to the Gaussian curvature  $G = C_1C_2$  as introduced in Equation (3). Indeed, for a closed membrane surface, the Gauss–Bonnet theorem of differential geometry implies the simple relationship

$$\int dAG = \int dAC_1C_2 = 2\pi\chi \quad (52)$$

between the area integral over the Gaussian curvature  $G$  and the Euler characteristic  $\chi$ . In the context of membrane elasticity, one may then consider the additional curvature energy<sup>[59]</sup>

$$E_G = \kappa_G \int dAG = 2\pi\chi\kappa_G \quad (53)$$

which involves the Gaussian curvature modulus  $\kappa_G$ . This modulus has the physical units of an energy and thus the same physical units as the bending rigidity  $\kappa$ .

The Gaussian curvature modulus is difficult to measure. Stability arguments indicate that  $-2 < \kappa_G/\kappa < 0$  for phospholipid vesicles.<sup>[123]</sup> Furthermore, both experimental<sup>[124,125]</sup> and simulation<sup>[126]</sup> studies indicate that the Gaussian curvature modulus  $\kappa_G$  is indeed negative and that its magnitude  $|\kappa_G|$  is roughly equal to the bending rigidity  $\kappa$ . Therefore, one expects that  $\kappa_G \simeq -\kappa \simeq -10^{-19}$  J. The Gaussian curvature energy  $E_G$  of a membrane compartment as given by Equation (53) does not depend explicitly on the membrane tension but will, in general, depend implicitly on this tension via the Gaussian curvature modulus  $\kappa_G$ .

The simple relation between the area integral over the Gaussian curvature  $G$  and the Euler characteristic  $\chi$  as given by Equation (52) applies to a closed membrane surface with uniform molecular composition and, thus, uniform elastic properties. This relation becomes more complex when the membrane contains domain boundaries<sup>[35,107,112]</sup> or when it involves bilayer pores or edges. In these cases, the area integral over the Gaussian curvature gives an additional term for each domain boundary and for each bilayer edge. Each of these terms is proportional to the line integral over the geodesic curvature<sup>[57]</sup> along the domain boundary or bilayer edge.

## 7.2. Curvature-Induced Fission of Membranes

Curvature-induced fission of membranes has been recently observed for giant vesicles exposed to His-tagged proteins in the exterior solution.<sup>[29]</sup> The binding of these proteins to NTA anchor lipids made it possible to control the spontaneous curvature in a precise manner, as described by Equation (9). In this way, we were able to transform prolate vesicles into dumbbells with a closed neck, see the first two images in Figure 25. The spontaneous curvature was then further increased by increasing the molar GFP concentration, which led to the cleavage of the membrane neck and the division of the vesicle. This process directly demonstrates that the spontaneous curvature generates a substantial constriction force at the membrane neck, see Figure 15.

The fission process involves the closure and subsequent cleavage of the membrane neck, as shown schematically in Figure 26a–c, where we depict the fission process of a small nanovesicle in order to explicitly resolve the lipid bilayer. The

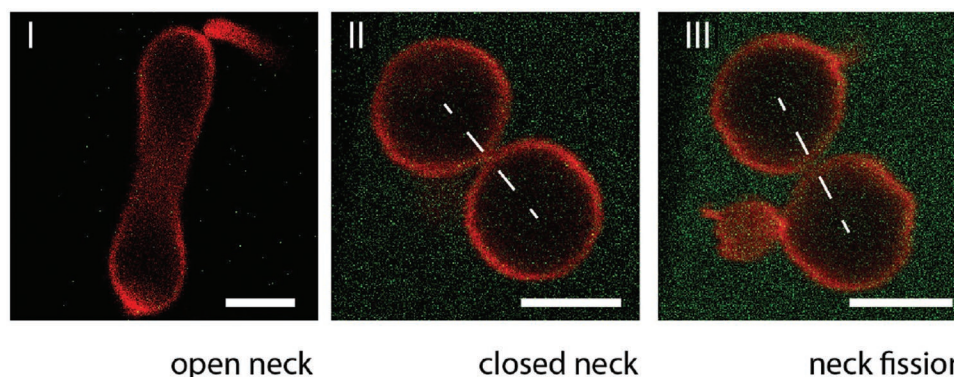


**Figure 25.** Curvature-induced fission of a giant vesicle: Transformation of a dumbbell-shaped vesicle with an open membrane neck into a two-sphere vesicle with a closed neck, and subsequent neck fission and vesicle division by increasing the molar concentration of His-tagged GFP in the exterior buffer.<sup>[29]</sup> The GFP binds to anchor lipids in the outer leaflet of the vesicle membrane, thereby generating a surprisingly large positive spontaneous curvature. This curvature generates a sufficiently large constriction force, compare Figure 15, which is consistent with the large negative mechanical tension in the same parameter regime. Reproduced under terms of the CC-BY license.<sup>[29]</sup> Copyright 2020, The Authors, published by Springer Nature.

neck cleavage has to overcome a free energy barrier arising from the local disruption of the bilayer structure. On the supramolecular scale, one may envisage this barrier for neck fission to arise from a cut across the bilayer and the creation of two ring-like hydrophobic bilayer edges across the neck. The “healing” of these bilayer edges then leads to two separate daughter vesicles. The mechanical work of fission is proportional to the total length of the bilayer edges. This length is minimal if the bilayer is cleaved across the neck.

The free energy landscape corresponding to such an exergonic or “downhill” fission process is displayed in Figure 26d. In this case, the free energy of the two-vesicle state is lower than the free energy of the dumbbell with a closed membrane neck, and the free energy difference  $\Delta_{21}$  in Figure 26d is negative. The fission rate, on the other hand, is governed by the positive free energy barrier  $\Delta_{1b}$  that the process has to overcome before it can be completed.

The observed fission of membrane necks as displayed in Figure 25 has several implications for the free energy landscape in Figure 26. First, from a comparison of the two vesicle shapes

before and after fusion in Figure 26a,c, we can conclude that the fission process involves only a relatively small change in the bending energy of the vesicle membrane. It then follows that, during neck fission, the contribution of the curvature energy to the free energy difference  $\Delta_{21}$  is dominated by the change in the Gaussian curvature energy  $E_G$  as defined in Equation (53). This energy change is given by  $\Delta E_G = 2\pi\Delta\chi\kappa_G = 4\pi\kappa_G$ . Furthermore, the observed fission process represents a spontaneous or exergonic process, which implies that the bending modulus  $\kappa_G$  is negative, in agreement with previous conclusions,<sup>[123–126]</sup> provided we can ignore changes in the elastic stretching energy of the membrane. As mentioned, before fission, the mechanical tension of the dumbbell-shaped vesicle is negative and the vesicle membrane is compressed.

The mechanism of curvature-induced fission of small nanovesicles as schematically depicted in Figure 26 provides an explanation for some early simulation results.<sup>[43,44]</sup> In one of these studies,<sup>[43]</sup> the nanovesicle was exposed to two different types of water beads in the interior and exterior compartment. The associated spontaneous curvature is likely to generate a

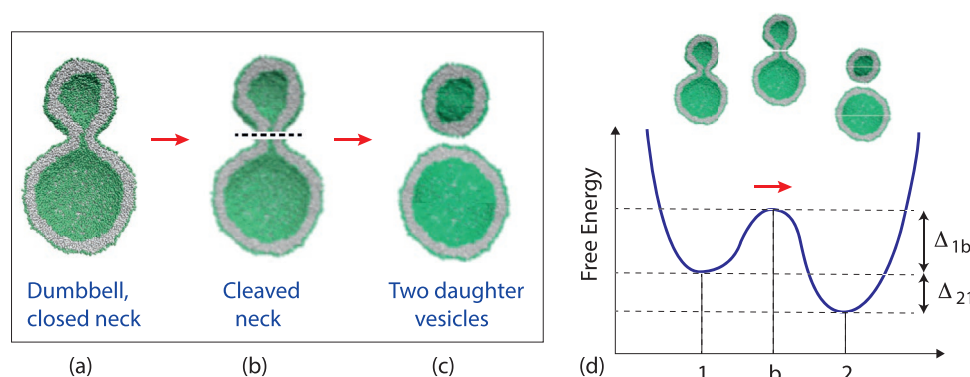


**Figure 26.** Fission of small nanovesicle and corresponding free energy landscape: Schematic fission process which a) starts from a dumbbell with a closed neck, b) proceeds via the cleavage of this neck, corresponding to the shortest possible cut (broken line) across the vesicle membrane, and c) ends up with two separate daughter vesicles. The cut leads to two circular membrane edges which have a positive edge tension and determine the free energy barrier; and d) Schematic free energy landscape versus an abstract reaction coordinate, with the free energy barrier provided by the cleaved neck. For the fission process to be “downhill” (exergonic) in free energy, the free energy difference  $\Delta_{21}$  between the two vesicle state 2 and the dumbbell state 1 must be negative. For  $\Delta_{21} < 0$ , the fission process can proceed without being coupled to another process such as nucleotide hydrolysis. The velocity or rate of the fission process, on the other hand, is determined by the positive free energy barrier  $\Delta_{1b}$ .

constriction force that can be sufficiently large to cleave the neck as predicted theoretically<sup>[58,89]</sup> and as observed experimentally for giant vesicles.<sup>[29]</sup> The latter mechanism should also apply to the fission of one-component monolayers of asymmetric block copolymers which has also been observed in molecular simulations.<sup>[44]</sup>

The curvature-induced constriction force at a membrane neck is described by the force–curvature relationships in Equations (18) and (19) for interior and exterior necks, respectively. These relationships are local and apply to all possible types of membrane necks between large and small spheres, provided we replace the neck curvature  $M_{ne}$  by the neck curvatures  $M_{ll}$ ,  $M_{ls}$ ,  $M_{ss}$ , or  $M_{**}$ , depending on the type of neck under consideration. For positive spontaneous curvature, the different neck curvatures are ordered according to  $M_{ll} < M_{ls} < M_{ss}$  as in Equation (47). Because the constriction forces at the different necks are proportional to  $m - M_{ne}$ , the  $ll$  necks experience the largest constriction forces.

### 7.3. Adhesion-Induced Fission of Nanovesicles

Using molecular simulations, we recently observed the budding and fission of nanovesicles, induced by the adsorption of small solutes onto the vesicle membranes.<sup>[17]</sup> Low concentrations of these solutes were present in the exterior aqueous solution and formed an adsorption layer on the outer leaflet of the vesicle membrane. This adsorption layer generated a significant spontaneous curvature that could be used to change the morphology of the vesicles. In addition to the solute concentration, we identified the solvent conditions as a second key parameter for these processes. By definition, good solvent conditions imply that the solution remains spatially uniform for all solute concentrations. A poor solvent, on the other hand, leads to a certain range of solute concentrations in which the solution undergoes liquid–liquid phase separation. Examples for this kind of phase behavior are provided by aqueous two-phase systems,<sup>[47,51,52]</sup> by water-in-water emulsions,<sup>[48]</sup> and by biomolecular condensates.<sup>[49,50]</sup>

For *good* solvent conditions, the budding of a nanovesicle can be controlled by reducing the vesicle volume for constant solute concentration or by increasing the solute concentration for constant vesicle volume. After the budding process has been completed, the budded vesicle consists of two membrane subcompartments which are connected by a closed membrane neck. The budding process is reversible as can be demonstrated explicitly by reopening the closed neck via a decrease of the solute concentration. For *poor* solvent conditions, on the other hand, we observe two unexpected morphological transformations of nanovesicles, as shown by the simulation snapshots in **Figure 27**. Close to the binodal line, at which the aqueous solution undergoes phase separation, the vesicle exhibits recurrent shape changes with closed and open membrane necks, see the simulation snapshots in **Figure 27a**, which cover a time period of about 35  $\mu$ s and are reminiscent of the flickering fusion pores (kiss-and-run) that have been observed for synaptic vesicles.<sup>[127–129]</sup>

As we approach the binodal line even closer, the recurrent shape changes are truncated by the fission of the membrane neck which leads to the division of the nanovesicle into two

daughter vesicles, see the simulation snapshots in **Figure 27b**, which cover a relatively short time period of less than a microsecond and show the last neck closure and the subsequent fission event. Inspection of **Figure 27b** reveals that the underlying fission mechanism is provided by the solute-mediated adhesion of the two membrane segments close to the neck, which leads to a growing, non-axisymmetric contact area between these two segments. In this way, our simulations reveal a nanoscale mechanism for the budding and fission of nanovesicles, a mechanism that arises from the interplay between membrane elasticity and solute-mediated membrane adhesion.

### 7.4. Tension-Induced Fusion of Membranes

Some time ago, we used molecular dynamics simulations to study the fusion of lipid bilayers on the nanoscale and its dependence on bilayer tension.<sup>[130–132]</sup> We observed a variety of pathways including hemifusion and bilayer rupture but we always found a range of positive bilayer tensions that led to fusion. One example for such a fusion process induced by bilayer tension is displayed in **Figure 28a–c**, which corresponds to two nanovesicles with a diameter of about 22 nm under a relatively high bilayer tension.<sup>[132]</sup> In this example, the fusion process proceeds in three steps. After about 260 ns as shown in **Figure 28c**, the two nanovesicles adhere to each other and form a relatively small contact area. After about 360 ns, the two adhering bilayers become disrupted, see **Figure 28b**, and then form, after about 400 ns, an open fusion pore that connects the two subcompartments in **Figure 28a**. The schematic free energy landscape corresponding to such an exergonic or “downhill” fusion process is displayed in **Figure 26d**.

#### 7.4.1. Leaflet versus Bilayer Tensions

In the fusion simulations just described, we did not resolve the leaflet tensions of the bilayers. Thus, we observed fusion of nanovesicles induced by a positive bilayer tension. Preliminary simulations provide evidence that we can also obtain fusion for tensionless bilayers, for which the outer leaflet tension is stretched and the inner leaflet is compressed, corresponding to positive outer leaflet tension and negative inner leaflet tension. Therefore, the leaflet tensions seem to provide another control parameter for the fusion of membranes.

#### 7.4.2. Comparison with the Fusion of Liquid Droplets

It is interesting to note that the tension-induced fusion of two vesicles is, to some extent, similar to the coalescence of two liquid droplets, which is driven by the reduction of interfacial area. Consider two spherical liquid droplets of a certain liquid phase with volumes  $V_1$  and  $V_2$  and interfacial areas  $A_1$  and  $A_2$ . When the two droplets coalesce for fixed total volume  $V_1 + V_2$ , the interfacial area  $A_{12}$  of the merged droplets will be smaller than the combined interfacial area  $A_1 + A_2$  of a two original droplets. Likewise, the interfacial free energy, which is equal to interfacial area times interfacial tension, is also reduced by

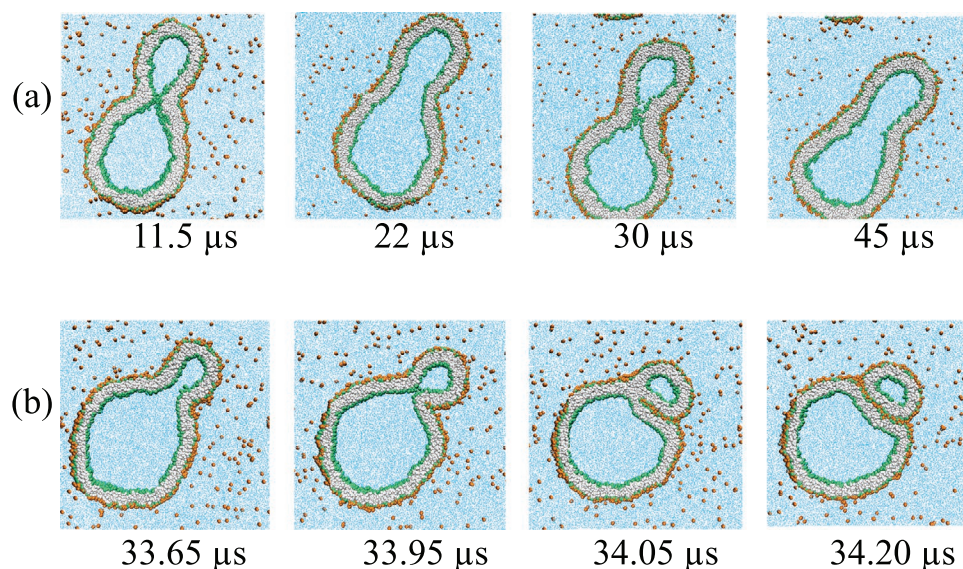


**Figure 27.** Unusual morphological transitions of nanovesicles exposed to small solutes (orange dots) in the exterior aqueous solution (blue), for low solute concentrations  $\Phi$  and poor solvent conditions. The cross-sections of the vesicle membranes depict lipid bilayers with green head groups and grey hydrocarbon chains. The solutes form adsorption layers (orange-green) at the outer leaflets of the bilayers: a) Time series of budded nanovesicle with recurrent shape changes between dumbbells with open and closed necks for solute mole fraction  $\Phi = 0.025$ ; and b) Division of nanovesicle by fission of the membrane neck for  $\Phi = 0.026$ , which leads to two daughter vesicles that adhere via the adsorbed solutes. Reproduced under terms of the CC-BY license.<sup>[17]</sup> Copyright 2021, The Authors, published by American Chemical Society.

droplet coalescence because the interfacial tension is a size-independent material parameter. However, both the bilayer tension and the leaflet tensions of membranes depend on the size and the shape of the membrane, as explicitly demonstrated for multispherical vesicles, see Equation (50). Furthermore, the membrane tension will also affect the Gaussian curvature modulus. Therefore, tension-induced fusion of membranes is more subtle and not really analogous to the fusion of droplets.

## 8. Summary and Outlook

In this paper, we described recent results about the remodeling of biomembranes, combining experimental observations on

giant vesicles and molecular dynamics simulations of small nanovesicles with the theory of membrane elasticity. Two types of remodeling processes have been distinguished. First, the remodeling of membrane shape for a given membrane topology has been addressed and, second, the remodeling of membrane topology, which is coupled to membrane fission and membrane fusion.

The remodeling of membrane shape leads to a striking polymorphism both for giant vesicles (Figures 2–6) and for small nanovesicles (Figures 7 and 8). This polymorphism can be understood from the interplay of curvature elasticity and membrane tension. For a given membrane area, the curvature elasticity of vesicles is determined by two dimensionless shape parameters, the rescaled spontaneous curvature and the rescaled vesicle volume as defined in Equations (22) and (23). The

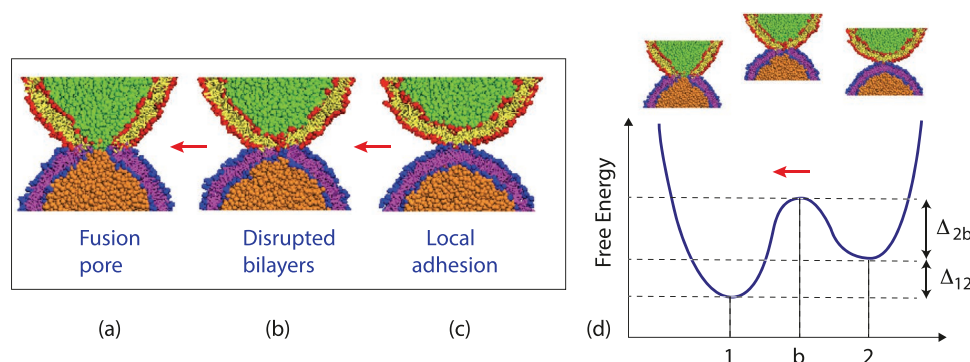


**Figure 28.** Tension-induced fusion of two spherical nanovesicles with a diameter of 22 nm. The lipids, that are initially assembled in the two vesicles, are distinguished by different colors, even though they are identical: a–c) The process starts in (c) from two vesicles that form a local adhesive contact, proceeds with the disruption of the two adhering bilayers in (b), and ends up in (a) with the opening of the fusion pore. The process from (c) to (a) takes about 140 ns.<sup>[132]</sup>; and d) Schematic free energy landscape versus an abstract reaction coordinate, with the free energy barrier corresponding to the disrupted bilayers within the adhesive contact. Reproduced with permission.<sup>[132]</sup> Copyright 2008, Royal Society of Chemistry.

spontaneous curvature can be generated by many membrane-bound molecules and nanostructures (Figure 9). This curvature-elastic parameter has been determined for a variety of giant vesicle systems as summarized by Table 1 and Equation (9). An unprecedented control over the spontaneous curvature has been recently achieved using nanomolar concentrations of His-tagged GFP, see Figure 3 and Equation (9). The underlying molecular mechanisms, which are responsible for this large curvature generation, remain to be identified. One complication is that the binding of His-tagged molecules depends strongly on the pH of the aqueous solution (S.Pramanik, J.Steinkühler, R. Dimova, J. Spatz, R. Lipowsky, Binding of His-tagged molecules to lipid membranes and giant vesicles; unpublished),

The spontaneous curvature determines the spontaneous membrane tension  $\sigma = 2\kappa m^2$ , which is a material parameter and represents the intrinsic tension scale of curvature elasticity.<sup>[88]</sup> Depending on the spontaneous curvature  $m$  and the bending rigidity  $\kappa$ , the spontaneous tension  $\sigma$  can vary between  $10^{-4}$  and  $1 \text{ mN m}^{-1}$ , as follows from the numerical values in Table 1 and from those based on Equation (9). Using micropipette experiments (Figure 10), the spontaneous tension has been directly measured for the compositional transbilayer asymmetry generated by the glycolipid (ganglioside) GM1.

The total membrane tension across the whole bilayer is equal to the sum of the spontaneous tension  $\sigma = 2\kappa m^2$  and the mechanical tension  $\Sigma$ . In contrast to the spontaneous tension, the mechanical tension  $\Sigma$  depends on both the shape and on the size of the membrane compartment. This dependence can be explicitly computed for two-sphere and multisphere vesicles, see Equations (37) and (50). The mechanical bilayer tension  $\Sigma$  can be further decomposed into two leaflet tensions as in Equation (10). One important conclusion about the leaflet tensions is that, in the absence of lipid flip-flops, these tensions can be quite significant even if the bilayer tension vanishes, see the examples in Figure 11. In the presence of frequent flip-flops, a planar bilayer with three lipid components has been observed to attain tensionless leaflets<sup>[99]</sup> as one might expect intuitively (Figure 12). However, the relaxation process of the leaflet tensions is difficult to monitor and has not been observed in another simulation study of multi-component bilayers.<sup>[102]</sup> Another open issue is the time-dependent relaxation of the leaflet tensions in small nanovesicles.

The theory of membrane elasticity was then used to elucidate the local properties of membrane necks. First, the neck curvature  $M_{\text{ne}}$  was defined in Equations (13) and (14) for interior and exterior necks. Using this neck curvature, two simple but important local relationships describe the stability of closed necks (Equations 15 and 16) and the constriction forces that act to squeeze these necks (Equations 18 and 19).

We used the closed neck relations, together with the area and volume relations (Equation 25), to determine the stability regimes of two-sphere vesicles (Figure 18). Inspection of this figure shows that the mechanical tension is large and negative for large positive and negative spontaneous curvatures, in accordance with the constriction forces. Two-sphere vesicles are special because they involve only a single type of membrane neck. In contrast, multispheres can involve up to three different types of necks that satisfy different stability relations. The overall stability of a certain multisphere is then determined

by the least stable neck. Multispherical shapes nicely illustrate the morphological complexity of membrane compartments (Figures 19–22).

The formation of membrane necks is also essential for the remodeling of membrane topology via membrane fission and fusion events. This kind of remodeling can be described in a very general manner in terms of the Euler characteristic  $\chi$  of the membrane compartments (Equation 51 and Figure 24). Single fission events increase the Euler characteristic by  $\Delta\chi = +2$  whereas single fusion events decrease it by  $\Delta\chi = -2$ . These changes in the Euler characteristic lead to changes in the Gaussian curvature energy (Equation 53), which are proportional to the Gaussian curvature modulus. If this modulus is negative, the curvature energy decreases during fission and increases during fusion. Thus, if the contribution of the elastic stretching energy to the free energy landscape could be ignored, we would conclude that fission is a spontaneous process whereas fusion is not. This conclusion agrees with the experimental observation that fission can be induced by increasing the spontaneous membrane curvature using low densities of membrane-bound proteins (Figure 25).

On the other hand, the elastic stretching energy seems to make a significant contribution to the free energy landscape for the adhesion-induced fission of nanovesicles (Figure 27) which leads to two adhering daughter vesicles that experience a positive mechanical tension. Furthermore, the tension-induced fusion of small nanovesicles (Figure 28) implies that the fusion process is downhill in the presence of a sufficiently large positive membrane tension. Thus, the relative contributions of curvature elasticity and tension during these fission and fusion processes remain to be clarified and represent an interesting topic for further studies.

The remodeling of membrane shape and topology provides many more challenges to be addressed in the future. In the context of multispherical vesicles, we would like to develop experimental methods by which we could obtain specific multispheres “on demand.” Likewise, it should be rather interesting to see how the multispheres respond to external forces and constraints in order to open and close the membrane necks in a controlled manner. Analogous remodeling processes should be accessible to giant vesicles with liquid-ordered and liquid-disordered domains (Figure 4). Using appropriate anchor lipids for the His-tagged proteins, it seems possible to obtain different spontaneous curvatures within the different domains. These different spontaneous curvatures, together with the line tension of the domain boundaries, will have a strong effect on the remodeling of the vesicle morphologies. In particular, it should be possible to spatially localize fusion and fission processes at the domain boundaries or within certain domains. Finally, it will be rather interesting to construct synthetic membrane systems that couple membrane fission and fusion events to active processes such as the shape oscillations in Figure 5.

## Acknowledgements

The author thanks all collaborators for enjoyable and fruitful interactions as well as the Max Planck School Matter to Life for a stimulating scientific environment. The manuscript is based on a talk that the author gave in the context of the Matter to Life Lecture Series.

Open access funding enabled and organized by Projekt DEAL.

## Conflict of Interest

The author declares no conflict of interest.

## Keywords

fission, fusion, membrane elasticity, membranes, synthetic biosystems, vesicles

Received: June 3, 2021

Revised: September 4, 2021

Published online: December 3, 2021

- [1] J. S. Bonifacino, B. S. Glick, *Cell* **2004**, *116*, 153.
- [2] J. Nixon-Abell, C. J. Obara, A. V. Weigel, D. Li, W. R. Legant, C. S. Xu, H. A. Pascolli, K. Harvey, H. F. Hess, E. Betzig, C. Blackstone, J. Lippincott-Schwartz, *Science* **2016**, *354*, aaf3928.
- [3] H. Wu, P. Carvalho, G. K. Voeltz, *Science* **2018**, *361*, 466.
- [4] L. Dreier, T. A. Rapoport, *J. Cell Biol.* **2000**, *148*, 883.
- [5] R. E. Powers, S. Wang, T. Y. Liu, T. A. Rapoport, *Nature* **2017**, *543*, 257.
- [6] R. Lipowsky, E. Sackmann (Eds), *Structure and Dynamics of Membranes, Handbook of Biological Physics*, Vol. 1, Elsevier, Amsterdam **1995**.
- [7] P. Bassereau, P. Sens (Eds), *Physics of Biological Membranes*, Springer Nature, Basingstoke, UK **2018**.
- [8] R. Dimova, C. Marques (Eds), *The Giant Vesicle Book*, Taylor & Francis, Milton Park, UK **2020**.
- [9] R. Lipowsky, R. Dimova, *Soft Matter* **2021**, *17*, 214.
- [10] U. Baxa, in *Characterization of Nanoparticles Intended for Drug Delivery* (Eds: S. E. McNeil), *Methods in Molecular Biology*, Vol. 1682, Springer Science+Business Media, Berlin **2018**, Ch. 6, pp. 73–88.
- [11] B. L.-S. Mui, P. R. Cullis, E. A. Evans, T. D. Madden, *Biophys. J.* **1993**, *64*, 443.
- [12] B. L.-S. Mui, H.-G. Döbereiner, T. D. Madden, P. R. Cullis, *Biophys. J.* **1995**, *69*, 930.
- [13] P. M. Frederik, D. H. W. Hubert, *Cryoelectron Microscopy of Liposomes*, Vol. 391, Elsevier, Amsterdam **2005**.
- [14] N. Dragicevic-Curic, D. Scheglmann, V. Albrecht, A. Fahr, *J. Control. Release* **2008**, *127*, 59.
- [15] D. Danino, *Curr. Opin. Colloid Interface Sci.* **2012**, *17*, 316.
- [16] R. Ghosh, V. Satarifard, A. Grafmüller, R. Lipowsky, *Nano Lett.* **2019**, *19*, 7703.
- [17] R. Ghosh, V. Satarifard, A. Grafmüller, R. Lipowsky, *ACS Nano* **2021**, *15*, 7237.
- [18] L. Qu, Y. Akbergenova, Y. Hu, T. Schikorski, *J. Comp. Neurol.* **2009**, *514*, 343.
- [19] B. R. Hopiavuori, L. D. Bennett, R. S. Brush, M. J. V. Hook, W. B. Thoreson, R. E. Anderson, *OCL: Oilseeds Fats Crops Lipids* **2016**, *23*, D113.
- [20] R. M. Johnstone, M. Adam, J. R. Hammond, L. Orr, C. Turbide, *J. Biol. Chem.* **1987**, *262*, 9412.
- [21] M. Simons, G. Raposo, *Curr. Opin. Cell Biol.* **2009**, *21*, 575.
- [22] P. I. Hanson, A. Cashikar, *Annu. Rev. Cell Dev. Biol.* **2012**, *28*, 337.
- [23] L. Barile, G. Vassalli, *Pharmacol. Therapeut.* **2017**, *174*, 63.
- [24] C. Lässer, S. C. Jang, J. Lötvall, *Mol. Aspects Med.* **2018**, *60*, 1.
- [25] S. G. Antimisiaris, S. Mourtas, A. Marazioti, *Pharmaceutics* **2018**, *10*, 218.
- [26] L. Han, E. W.-F. Lam, Y. Sun, *Mol. Cancer* **2019**, *18*, 59.
- [27] A. M. Valm, S. Cohen, W. R. Legant, J. Melunis, U. Hershberg, E. Wait, A. R. Cohen, M. W. Davidson, E. Bethig, J. Lippincott-Schwartz, *Nature* **2017**, *547*, 162.
- [28] T. Bhatia, S. Christ, J. Steinkühler, R. Dimova, R. Lipowsky, *Soft Matter* **2020**, *16*, 1246.
- [29] J. Steinkühler, R. L. Knorr, Z. Zhao, T. Bhatia, S. Bartelt, S. Wegner, R. Dimova, R. Lipowsky, *Nature Commun.* **2020**, *11*, 905.
- [30] C. Dietrich, L. Bagatolli, Z. Volovyk, N. Thompson, M. Levi, K. Jacobson, E. Gratton, *Biophys. J.* **2001**, *80*, 1417.
- [31] S. Veatch, S. Keller, *Biophys. J.* **2003**, *85*, 3074.
- [32] T. Baumgart, S. Hess, W. Webb, *Nature* **2003**, *425*, 821.
- [33] N. Bezlyepkina, R. S. Graciá, P. Shchelokovskyy, R. Lipowsky, R. Dimova, *Biophys. J.* **2013**, *104*, 1456.
- [34] R. Lipowsky, *J. Phys. II France* **1992**, *2*, 1825.
- [35] F. Jülicher, R. Lipowsky, *Phys. Rev. Lett.* **1993**, *70*, 2964.
- [36] K. A. Riske, N. Bezlyepkina, R. Lipowsky, R. Dimova, *Biophys. Rev. Lett.* **2006**, *1*, 387.
- [37] Y. Dreher, K. Jahnke, E. Bobkova, J. P. Spatz, K. Göpfrich, *Angew. Chem., Int. Ed.* **2021**, *60*, 10661.
- [38] T. Litschel, B. Ramm, R. Maas, M. Heymann, P. Schwille, *Angew. Chem., Int. Ed.* **2018**, *57*, 16286.
- [39] S. Christ, T. Litschel, P. Schwille, R. Lipowsky, *Soft Matter* **2021**, *17*, 319.
- [40] Z. Hu, E. P. Gogol, J. Lutkenhaus, *Proc. Natl. Acad. Sci.* **2002**, *99*, 6761.
- [41] J. Shillcock, R. Lipowsky, *J. Phys. Cond. Mat* **2006**, *18*, S1191.
- [42] K. A. Smith, D. Jasnow, A. C. Balazs, *J. Chem. Phys.* **2007**, *127*, 084703.
- [43] A. J. Markvoort, P. Spijker, A. F. Smeijers, K. Pieterse, R. A. van Santen, P. A. J. Hilbers, *J. Phys. Chem. B* **2009**, *113*, 8731.
- [44] X. Li, Y. Liu, L. Wang, M. Deng, H. Liang, *Phys. Chem. Chem. Phys.* **2009**, *11*, 4051.
- [45] N. Urakami, T. Jimbo, Y. Sakuma, M. Imai, *Soft Matter* **2018**, *14*, 3018.
- [46] V. Satarifard, A. Grafmüller, R. Lipowsky, *ACS Nano* **2018**, *12*, 12424.
- [47] P. A. Albertsson, *Partition of Cell Particles and Macromolecules: Separation and Purification of Biomolecules, Cell Organelles Membranes, and Cells in Aqueous Polymer Two-phase Systems and their Use in Biochemical Analysis and Biotechnology*, 3rd ed., Wiley, Hoboken, NJ, **1986**.
- [48] J. Esquena, *Curr. Opin. Colloid Interface Sci.* **2016**, *25*, 109.
- [49] C. P. Brangwynne, C. R. Eckmann, D. S. Courson, A. Rybarska, C. Hoegel, J. Gharakhani, F. Jülicher, A. A. Hyman, *Science* **2009**, *324*, 1729.
- [50] S. F. Banani, H. O. Lee, A. A. Hyman, M. K. Rosen, *Nature Rev.: Mol. Cell Biol.* **2017**, *18*, 285.
- [51] Y. Li, R. Lipowsky, R. Dimova, *JACS* **2008**, *130*, 12252.
- [52] R. Dimova, R. Lipowsky, *Adv. Mater. Interf.* **2017**, *4*, 1600451.
- [53] R. Lipowsky, *J. Phys. Chem. B* **2018**, *122*, 3572.
- [54] R. Lipowsky, in *Physics of Biological Membranes* (Eds: P. Bassereau, P. Sens), Springer, Berlin **2018**, pp. 1–44.
- [55] R. Dimova, *Adv. Colloid Interface Sci.* **2014**, *208*, 225.
- [56] W. Rawicz, K. C. Olbrich, T. McIntosh, D. Needham, E. Evans, *Biophys. J.* **2000**, *79*, 328.
- [57] M. do Carmo, *Differential Geometry of Curves and Surfaces*, Prentice-Hall, Englewood Cliffs, NJ **1976**.
- [58] R. Lipowsky, in *The Giant Vesicle Book* (Eds: R. Dimova, C. Marques), Taylor & Francis, Milton Park, UK **2020**, Ch. 5, pp. 73–168.
- [59] W. Helfrich, *Z. Naturforsch.* **1973**, *28c*, 693.
- [60] U. Seifert, K. Berndl, R. Lipowsky, *Phys. Rev. A* **1991**, *44*, 1182.
- [61] B. W. van der Meer, in *Biomembranes: Physical Aspects* (Ed: M. Shinitzky), VCH Verlagsgesellschaft, Weinheim, Germany, **1993**, pp. 97–158.
- [62] J. Liu, J. C. Conboy, *Biophys. J.* **2005**, *89*, 2522.
- [63] J. Liu, K. L. Brown, J. C. Conboy, *Faraday Discuss.* **2013**, *161*, 45.
- [64] T. L. Steck, J. Ye, Y. Lange, *Biophys. J.* **2002**, *83*, 2118.
- [65] J. A. Hamilton, *Curr. Opin. Lipidol.* **2003**, *14*, 263.

- [66] R. J. Bruckner, S. S. Mansy, A. Ricardo, L. Mahadevan, J. W. Szostak, *Biophys. J.* **2009**, *97*, 3113.
- [67] P. F. Devaux, *Febs. Lett.* **1988**, *234*, 8.
- [68] T. T. Sebastian, R. D. Baldrige, P. Xu, T. R. Graham, *Biochim. Biophys. Acta* **2012**, *1821*, 1068.
- [69] H. M. Hankins, R. D. Baldrige, P. Xu, T. R. Graham, *Traffic* **2015**, *16*, 35.
- [70] Y. Yang, M. Lee, G. D. Fairn, *J. Biol. Chem.* **2018**, *293*, 6230.
- [71] U. Seifert, L. Miao, H.-G. Döbereiner, M. Wortis, in *The Structure and Conformation of Amphiphilic Membranes* (Eds: R. Lipowsky, D. Richter, K. Kremer), *Springer Proceedings in Physics*, Springer-Verlag, Berlin, **1992**, pp. 93–96.
- [72] H.-G. Döbereiner, E. Evans, M. Kraus, U. Seifert, M. Wortis, *Phys. Rev. E* **1997**, *55*, 4458.
- [73] R. Lipowsky, *Adv. Colloid Interface Sci.* **2014**, *208*, 14.
- [74] H. Deuling, W. Helfrich, *J. Physique* **1976**, *37*, 1335.
- [75] G. van Meer, D. R. Voelker, G. W. Feigenson, *Nature Rev.: Mol. Cell Biol.* **2008**, *9*, 112.
- [76] B. Fadeel, D. Xue, *Crit. Rev. Biochem. Mol. Biol.* **2009**, *44*, 264.
- [77] D. Marquardt, B. Geier, G. Pabst, *Membranes* **2015**, *5*, 180.
- [78] T. Bhatia, J. Agudo-Canalejo, R. Dimova, R. Lipowsky, *ACS Nano* **2018**, *12*, 4478.
- [79] R. Dasgupta, M. S. Miettinen, N. Fricke, R. Lipowsky, R. Dimova, *Proc. Nat. Acad. Sci. USA* **2018**, *115*, 5756.
- [80] M. Aureli, L. Mauri, M. G. Ciampa, A. Prinetti, G. Toffano, C. Secchieri, S. Sonnino, *Mol. Neurobiol.* **2016**, *53*, 1824.
- [81] C.-L. Schengrund, *Trends Biochemical. Sci.* **2015**, *40*, 397.
- [82] H. Ewers, W. Römer, A. E. Smith, K. Bacia, S. Dmitrieff, W. Chai, R. Mancini, J. Kartenbeck, V. Chambon, L. Berland, A. Oppenheim, G. Schwarzmann, T. Feizi, P. Schwille, P. Sens, A. Helenius, L. Johannes, *Nature Cell Biol.* **2010**, *12*, 11.
- [83] Y. Liu, J. Agudo-Canalejo, A. Grafmüller, R. Dimova, R. Lipowsky, *ACS Nano* **2016**, *10*, 463.
- [84] J. Agudo-Canalejo, R. Lipowsky, *ACS Nano* **2015**, *9*, 3704.
- [85] R. Lipowsky, *Europhys. Lett.* **1995**, *30*, 197.
- [86] R. Lipowsky, H. G. Döbereiner, C. Hiergeist, V. Indrani, *Physica A* **1998**, *249*, 536.
- [87] V. Nikolov, R. Lipowsky, R. Dimova, *Biophys. J.* **2007**, *92*, 4356.
- [88] R. Lipowsky, *Faraday Discuss.* **2013**, *161*, 305.
- [89] R. Lipowsky, Multiresponsive Behavior of Biomembranes and Giant Vesicles, *Advances in Biomembranes and Lipid Self-Assembly*, Vol. 30, Academic Press, Cambridge, MA **2019**, Ch. 3, pp. 105–155.
- [90] B. Rózycki, R. Lipowsky, *J. Chem. Phys.* **2015**, *142*, 054101.
- [91] A. Sreekumari, R. Lipowsky, *J. Chem. Phys.* **2018**, *149*, 084901.
- [92] R. P. Rand, A. C. Burton, *Biophys. J.* **1964**, *4*, 115.
- [93] R. M. Hochmuth, *J. Biomech.* **2000**, *33*, 15.
- [94] N. Samudrala, J. Nam, R. Sarfati, R. W. Style, E. R. Dufresne, *Phys. Rev. E* **2017**, *95*, 012805.
- [95] A. Tian, B. R. Capraro, C. Esposito, T. Baumgart, *Biophys. J.* **2009**, *97*, 1636.
- [96] M. Heinrich, A. Tian, C. Esposito, T. Baumgart, *PNAS* **2010**, *107*, 7208.
- [97] J. A. J. Arpino, P. J. Rizkallah, D. D. Jones, *PLOS One* **2012**, *7*, e47132.
- [98] B. Sorre, A. Callan-Jones, J. Manzi, B. Goud, J. Prost, P. Bassereau, A. Roux, *PNAS* **2012**, *109*, 173.
- [99] M. Miettinen, R. Lipowsky, *Nano Lett.* **2019**, *19*, 5011.
- [100] M. Winterhalter, W. Helfrich, *J. Phys. Chem.* **1992**, *96*, 327.
- [101] R. H. Templer, *Langmuir* **1995**, *11*, 334.
- [102] A. Hossein, M. Deserno, *Biophys. J.* **2020**, *118*, 624.
- [103] W. D. Bancroft, *J. Phys. Chem.* **1913**, *17*, 501.
- [104] W. Bancroft, C. Tucker, *J. Phys. Chem.* **1927**, *31*, 1681.
- [105] Other types of necks are possible<sup>[58]</sup> but will not be considered here for the sake of simplicity.
- [106] B. Fourcade, L. Miao, M. Rao, M. Wortis, R. Zia, *Phys. Rev. E* **1994**, *49*, 5276.
- [107] F. Jülicher, R. Lipowsky, *Phys. Rev. E* **1996**, *53*, 2670.
- [108] R. Lipowsky, *Biol. Chem.* **2014**, *395*, 253.
- [109] A. Roux, G. Koster, M. Lenz, B. Sorre, J.-B. Manneville, P. Nassoy, P. Bassereau, *PNAS* **2010**, *107*, 4242.
- [110] J. Schoeneberg, M. R. Pavlin, S. Yan, M. Righini, I.-H. Lee, L.-A. Carlson, A. H. Bahrami, D. H. Goldman, X. Ren, G. Hummer, C. Bustamante, J. H. Hurley, *Science* **2018**, *362*, 1423.
- [111] J. Xiao, E. D. Goley, *Curr. Opin. Microbiol.* **2016**, *34*, 90.
- [112] T. Baumgart, S. Das, W. W. Webb, J. T. Jenkins, *Biophys. J.* **2005**, *89*, 1067.
- [113] J. Agudo-Canalejo, R. Lipowsky, *Soft Matter* **2016**, *12*, 8155.
- [114] P. Bassereau, R. Jin, T. Baumgart, M. Deserno, R. Dimova, V. A. Frolov, P. V. Baskirov, H. Grubmüller, R. Jahn, H. J. Risselada, L. Johannes, M. M. Kozlov, R. Lipowsky, T. J. Pucadyil, W. F. Zeno, J. C. Stachowiak, D. Stamou, A. Breuer, L. Lauritsen, C. Simon, C. Sykes, G. A. Voth, T. R. Weikl, *J. Phys. D: Appl. Phys.* **2018**, *51*, 343001.
- [115] In practise, the diffusion of an *ls* neck is more difficult to monitor because of the rotational diffusion of the whole vesicle.
- [116] M. Terasaki, L. B. Chen, K. Fujiwara, *J. Cell. Biol.* **1986**, *103*, 1557.
- [117] C. Lee, L. B. Chen, *Cell* **1988**, *54*, 37.
- [118] E. N. Gilbert, H. O. Pollak, *SIAM J. Appl. Math.* **1968**, *16*, 1.
- [119] S. Hildebrandt, A. Tromba, *Mathematics and Optimal Form*, American Scientific Library, **1985**.
- [120] J. M. Smith, R. Weiss, M. Patel, *Networks* **1995**, *25*, 273.
- [121] H. J. Prömel, A. Steger, *The Steiner Tree Problem*, Vieweg - Springer, Berlin **2002**.
- [122] R. L. Knorr, R. Lipowsky, R. Dimova, *Autophagy* **2015**, *11*, 2134.
- [123] W. Helfrich, W. Harbich, In J. Meunier, D. Langevin, N. Bocara (Eds), *Physics of Amphiphilic Layers*, *Springer Proceedings in Physics*, Vol. 21, Springer-Verlag, Berlin, **1987**, pp. 58–63.
- [124] A. Derzhanski, A. G. Petrov, M. D. Mitov, *Ann. Phys.* **1978**, *3*, 297.
- [125] S. Lorenzen, R.-M. Servuss, W. Helfrich, *Biophys. J.* **1986**, *50*, 565.
- [126] M. Hu, J. J. Briguglio, M. Deserno, *Biophys. J.* **2012**, *102*, 1403.
- [127] R. Fesce, F. Grohovaz, F. Valtorta, J. Meldolesi, *Trends Cell Biol.* **1994**, *4*, 1.
- [128] R. G. W. Staal, E. V. Mosharov, D. Sulzer, *Nat. Neurosci.* **2004**, *7*, 341.
- [129] R. M. Wightman, C. L. Haynes, *Nat. Neurosci.* **2004**, *7*, 321.
- [130] J. Shillcock, R. Lipowsky, *Nat. Mater.* **2005**, *4*, 225.
- [131] A. Grafmüller, J. Shillcock, R. Lipowsky, *Phys. Rev. Lett.* **2007**, *98*, 218101.
- [132] L. Gao, R. Lipowsky, J. C. Shillcock, *Soft Matter* **2008**, *4*, 1208.



**Reinhard Lipowsky** obtained his PhD in 1982 at the University of Munich and then worked as a research associate at Cornell University, Upstate New York. In 1990, he was appointed full professor at the University of Cologne and director at the Forschungszentrum Jülich. Three years later, he became one of the founding directors of the Max Planck Institute of Colloids and Interfaces, Potsdam. He is a member of the Berlin-Brandenburg Academy of Sciences, has honorary professorships at the University of Potsdam and at Humboldt University, Berlin, and is a fellow of the Max Planck School Matter to Life, the main focus of his research.